The critical field of superconducting transition metal dichalcogenide monolayers

Kevin Choi (4705742) Supervisors: Lin Wang, Anton Akhmerov

June 4, 2019

Abstract

The purpose of this research is to investigate the critical field of superconducting transition metal dichalcogenide (TMD) monolayers MoX_2 (X = S, Se, or Te), in particular for chemical potentials where there is vanishing spin-orbit interaction (vanishing region). In general, it has been shown in research that Ising spin-orbit interaction in TMD monolayers enhances the critical field of the superconducting phase. One may therefore expect that the enhancement of the critical field will be suppressed when this spin-orbit interaction vanishes. In normal phase MoX_2 monolayers, it has been found that the band structure has a vanishing spin splitting near the bottom of the lowest conduction band. In this research, a $\mathbf{k} \cdot \mathbf{p}$ model of the conduction band has been used and superconductivity is described using Bogoliubov-De Gennes formalism. A numerical model has been formulated from this model and formalism, and the results show that there is indeed a suppression of the critical field for all 3 materials in the vanishing region. In relation with experiments, it also has been found there is a minimum chemical potential when the TMD monolayer becomes superconducting. For MoS_2 , this critical chemical potential is above the vanishing region which means a suppression of the critical field cannot be measured here. On the other hand, the critical chemical potentials of $MoSe_2$ and $MoTe_2$ do possibly lie below the vanishing region, but this requires that the temperature in experiment should be below 2 K. Next to the critical field, also the topological phases have been briefly investigated.

Contents

| 1 | Intr | oduction | 2 | | |
|---|--|--|----|--|--|
| 2 | Nor | rmal phase band structure | 4 | | |
| | 2.1 | Three-band tight binding model | 4 | | |
| | | 2.1.1 Onsite Hamiltonian | 4 | | |
| | | 2.1.2 Hopping integrals | 6 | | |
| | | 2.1.3 Spin-orbit interaction | 8 | | |
| | | 2.1.4 Results and discussion | 9 | | |
| | 2.2 | 11-band tight binding model | 10 | | |
| | | 2.2.1 Orbitals and hopping integrals | 10 | | |
| | | 2.2.2 Spin-orbit interaction | 11 | | |
| | | 2.2.3 Results and discussion | 11 | | |
| | 2.3 | $\mathbf{k} \cdot \mathbf{p}$ method around the $\pm \mathbf{K}$ point | 12 | | |
| | | 2.3.1 k · p model | 13 | | |
| | | 2.3.2 Spin-orbit interaction | 17 | | |
| | | 2.0.2 Spin of the Interaction | | | |
| 3 | | g superconductivity | 20 | | |
| | 3.1 | Basic theory on superconductivity | 20 | | |
| | | 3.1.1 Hamiltonian | 20 | | |
| | | 3.1.2 Obtaining the weak-coupling limit | 22 | | |
| | | 3.1.3 Universal critical temperature | 24 | | |
| | 3.2 | Critical magnetic field | 24 | | |
| | | 3.2.1 2D free electron model | 24 | | |
| | | 3.2.2 Superconducting TMD monolayers | 26 | | |
| | 3.3 | Topological phase | 26 | | |
| | 3.4 | Comparison with literature | 27 | | |
| 4 | Nime | merical model | 29 | | |
| * | 4.1 | Description of model | 29 | | |
| | 7.1 | 4.1.1 $\mathbf{k} \cdot \mathbf{p}$ parameters | 29 | | |
| | | 4.1.2 k-point generation | 30 | | |
| | | 4.1.3 Minimizing the free energy | 31 | | |
| | | 4.1.4 Finding the critical field | 32 | | |
| | 4.2 | | 32 | | |
| | 4.2 | Analysis of model | | | |
| | | 4.2.1 Practical input values | 32 | | |
| | | 4.2.2 Convergence in the weak coupling limit | 33 | | |
| | | 4.2.3 Uncertainty analysis | 33 | | |
| | 4.0 | 4.2.4 Free electron case | 34 | | |
| | 4.3 | Results and discussion | 34 | | |
| | | 4.3.1 Critical field | 34 | | |
| | | 4.3.2 Topological phase diagram | 36 | | |
| | | 4.3.3 Varying chemical potential and critical field, fixed temperature | 36 | | |
| | | 4.3.4 Varying temperature and critical field, fixed chemical potential | 36 | | |
| 5 | Con | nclusion | 39 | | |
| A | Convergence of Δ that minimizes free energy 4 | | | | |
| R | The | e relative uncertainty for MoSa and MoTea as function of resolution | 42 | | |

Chapter 1

Introduction

The main purpose of this research is to calculate the in-plane critical field of a superconducting transition metal dichalcogenide (TMD) monolayer by means of a numerical model. In this thesis, the theory of the TMD monolayer and a numerical model to calculate in-plane critical fields will be explained. TMD monolayers are semiconductors that have a structure of the form MX_2 and consist of a transition metal and two chalcogens. In general, a transition metal is any metal that has a partially filled d-shell, but this thesis will only focus on group 6 transition metals like molybdenum (Mo) and tungsten (W). A chalcogen, on the other hand, is a group 16 atom such as sulfur (S) or selenium (Se). Although oxygen (O) is technically a chalcogen as well, it will not be considered in this thesis, as it has very different chemical properties compared to other chalcogens. The crystal structure of group 6 TMD monolayers is displayed in fig. 1.1. As it can be seen in the 3D figure (fig. 1.1a), the transition metal atoms are sandwiched between two chalcogen layers and each layer has an equal number of atoms (hence MX_2). From the top view (fig. 1.1b), the structure is very similar to the honeycomb structure of graphene, except it does not have a point inversion symmetry in the bonds due to the alternation between two different atoms.

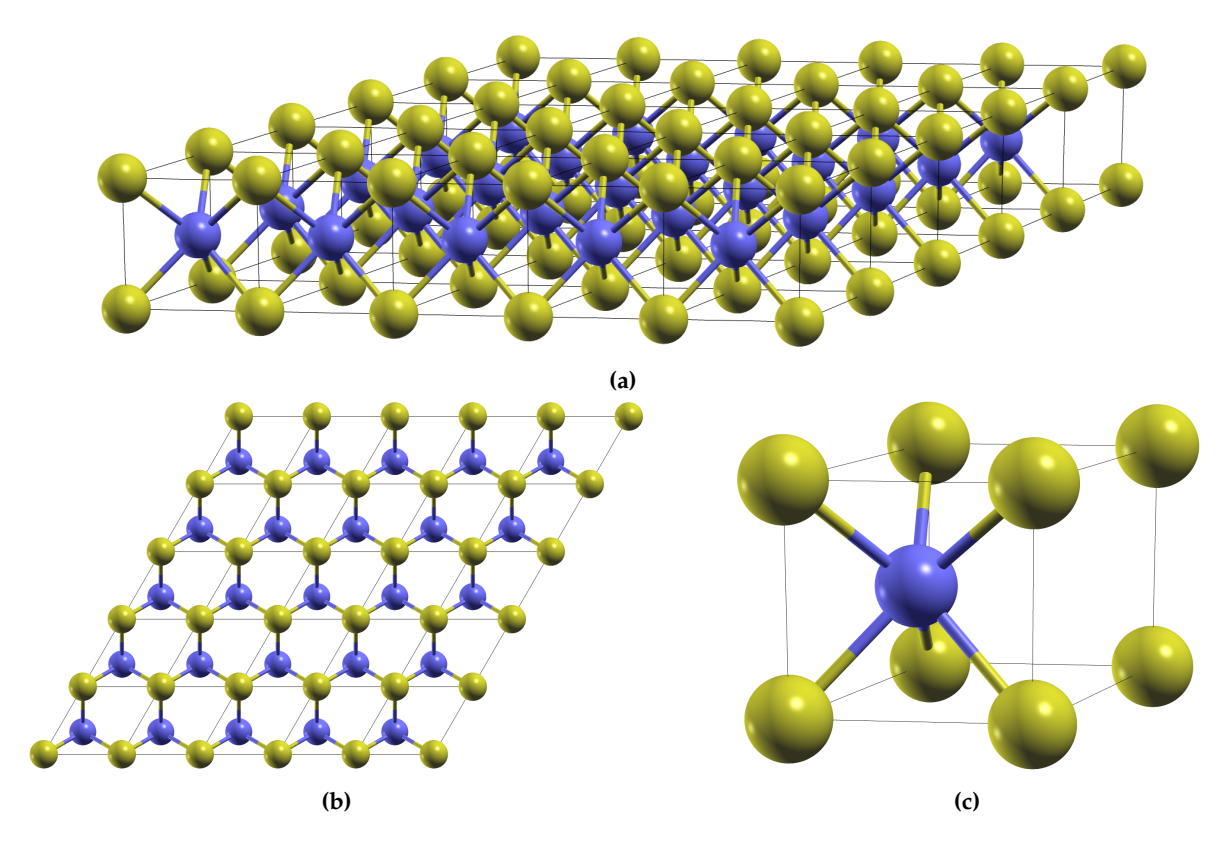


Figure 1.1: The crystal structure of a group 6 TMD monolayer with the transition metal in blue and the chalcogens in yellow. (a) 3D figure; (b) top view; (c) single unit cell. The figures are rendered with XCrysDen [1].

The history and research behind TMD monolayers is closely linked to that of graphene, which has been experimentally discovered by Geim and Novoselov in 2004 [2]. Not much later, Novoselov et al. demonstrated

the fabrication of other 2D materials like boron nitride and also some TMD monolayers like MoS₂ by means of a mechanical cleaving technique [3]. This technique is also used in follow-up experiments [4, 5]. It should be noted, however, that the technique is not scalable, although research has been done to improve this [6]. Since the experimental discovery of graphene, more and more research has been done on TMD monolayers (see also fig. 1 in ref. [7]).

One important property of TMD monolayer semiconductors is that they have a direct bandgap, which has also been found in experiments [4, 5]. This is different from bulk TMD, which has an indirect bandgap [8–10]. The direct band gap of TMD monolayers makes it suitable for several potential applications, such as field effect transistors [11] or photo-detectors [12]. Two other important properties of TMD monolayers are due to the lack of inversion symmetry. The first one is that the interaction between electrons and circular polarized light is valley-dependent [13, 14], which has potential for new type of devices called valleytronics [15]. The other one is the exhibition of Ising spin-orbit interaction (Ising SOI), which fixes the electron spin in the out-of-plane directions [16, 17]. This is different from Rashba spin-orbit interaction where the electron spins are in-plane.

This thesis will focus on the superconducting phase of TMD monolayers. When combining superconductivity with the Ising SOI of TMD monolayers, one will obtain Ising superconductors. It has been shown in experiments that TMD monolayers have an enhanced in-plane critical field [18]. This can be explained from the fact the Ising SOI interaction keeps the electron spins out-of-plane, effectively protecting the spins from aligning along an external in-plane magnetic field, which would break the superconductivity of the TMD monolayer. The focus of this thesis will be particularly on TMD monolayers with nodal topological superconductivity, introduced by Wang et al.[19] The source of this topology is the vanishing SOI at the lowest conduction band near the K point, which will be discussed in more detail in this thesis. It is expected that the critical field will be suppressed when the chemical potential crosses the vanishing spin-orbit interaction in the conduction band as a weaker SOC implies a weaker protection.

The contents of this thesis are as follows:

- in chapter 2, the band structure of TMD monolayers in the normal phase will be visualized, which will be needed to explain Ising superconductivity later;
- in chapter 3, Ising superconductivity will be explained in more detail using Bogoliubov-De Gennes formalism for conventional superconductors;
- in chapter 4, a numerical model will be presented to calculate the in-plane critical field for Ising superconducting TMD monolayers, using the concepts introduced in the previous chapter;
- finally, a conclusion about my research will be given in chapter 5.

Chapter 2

Normal phase band structure

In this chapter, the band structure of TMD monolayers in the normal phase will be discussed. The two tools that will be covered in this chapter to analyze the band structure are the tight binding model and the $\mathbf{k} \cdot \mathbf{p}$ method. In the first two sections, two different tight binding models based on earlier work will be introduced for the TMD monolayer: the three-band model and the 11-band model. The three-band model reasonably describes the three bands near the Fermi level, but does miss some important details of the conduction band that will be relevant in this thesis. Nevertheless, it is a good starting point to explain how tight binding models can be constructed. The 11-band model is more accurate and will also be used later in this thesis. The third section introduces the $\mathbf{k} \cdot \mathbf{p}$ method, which is an approximation of the band structure close to a particular \mathbf{k} -point in reciprocal lattice. This method provides simple but accurate description of the band structure around that point, which is very useful for analytical analysis.

2.1 Three-band tight binding model

The three-band model, based on work by Liu et al. [20], shows that the d_{z^2} , d_{xy} , and $d_{x^2-y^2}$ orbitals of the transition metal can provide a good description of the 3 bands near the Fermi level of a TMD monolayer. The d_{z^2} , d_{xy} , and $d_{x^2-y^2}$ orbitals (see fig. 2.1) are cubic harmonics and these are related to the spherical harmonics encountered in quantum mechanics when deriving the eigenstates of the angular momentum operator:

$$|d_{z^2}\rangle = \left|Y_2^0\right\rangle,\tag{2.1}$$

$$\left| d_{xy} \right\rangle = \frac{i}{\sqrt{2}} \left(\left| Y_2^{-2} \right\rangle - \left| Y_2^2 \right\rangle \right),\tag{2.2}$$

$$\left| d_{x^2 - y^2} \right\rangle = \frac{1}{\sqrt{2}} \left(\left| Y_2^{-2} \right\rangle + \left| Y_2^2 \right\rangle \right). \tag{2.3}$$

One consequence of the so-called three-band approximation is that a triangular lattice (see fig. 2.2a) can be used instead of a honeycomb lattice, as chalcogens atoms do not have to be considered. The three-band approximation is accurate near the +K and -K points if only nearest neighbor hoppings are considered. If second and third nearest neighbor hoppings are taken into account as well, a good description of the band structure in the entire Brillouin zone can be provided except near the Γ point (see fig. 2.2b). This is also the limitation of the three-band approximation, since p-orbitals of the chalcogens have a non-negligible contribution to the band structure at the Γ point.

2.1.1 Onsite Hamiltonian

In order to calculate the band structure, a Python package called Kwant [21] will be used to ease the work. This package requires to specify the onsite energies of the orbitals and all the possible hopping integrals between two orbitals at different sites. Hopping integrals will be discussed in section 2.1.2 in more detail. Using the basis $\{|d_{z^2}\rangle, |d_{xy}\rangle, |d_{x^2-y^2}\rangle\}$, the Hamiltonian of the onsite energies is simple and given by

$$\hat{H}_{onsite} = \begin{pmatrix} \varepsilon_1 & 0 & 0 \\ 0 & \varepsilon_2 & 0 \\ 0 & 0 & \varepsilon_2 \end{pmatrix}. \tag{2.4}$$

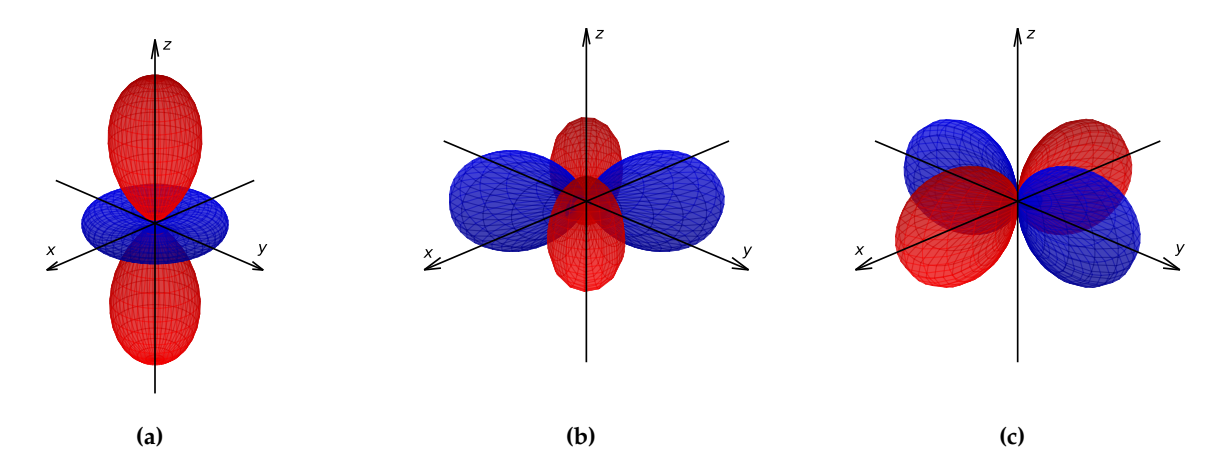


Figure 2.1: Plots of the d_{z^2} (a), d_{xy} (b), and $d_{x^2-y^2}$ (c) orbitals used in the three-band approximation.

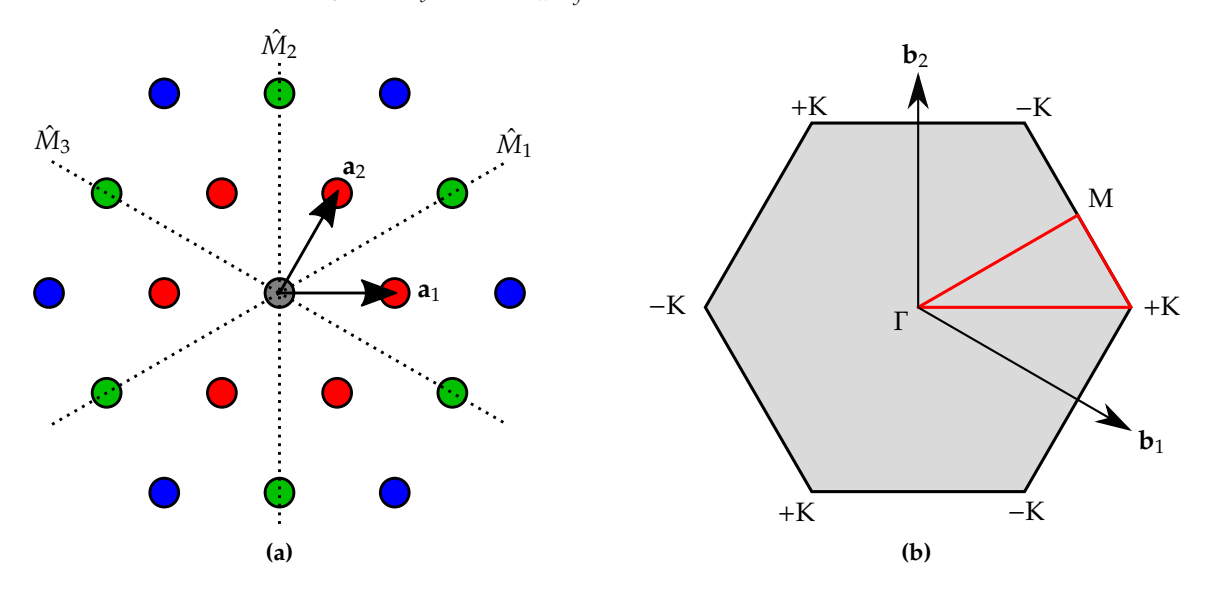


Figure 2.2: (a) the lattice of the transition metal atoms with primitive vectors \mathbf{a}_1 and \mathbf{a}_2 . The nearest neighbors (NN), second nearest neighbors (SNN) and third nearest neighbors (TNN) are the hoppings from the gray center to the red, green and blue dots respectively. The dotted lines indicate the mirror planes \hat{M}_1 , \hat{M}_2 , \hat{M}_3 ; (b) visualization of the first Brillouin zone of the transition metal lattice with reciprocal vectors \mathbf{b}_1 and \mathbf{b}_2 and high symmetry points Γ , M, +K, and -K.

The d_{xy} and $d_{x^2-y^2}$ orbitals have to be degenerate, which can be explained from the fact that a TMD monolayer has a D_{3h} point-group symmetry. It will become clear later how such a point-group symmetry leads to a degeneracy between these two orbitals. But first, consider some of the elements of the D_{3h} symmetry group:

- \hat{I} , the identity operation (i.e. do nothing).
- \hat{C}_3 , a counterclockwise rotation of $2\pi/3$ around the *z*-axis (i.e. the axis perpendicular to TMD monolayer).
- \hat{M}_i , a reflection in the mirror plane indicated by the lines visualized in fig. 2.2a.

To understand why symmetries can make quantum states degenerate (in this case, the d_{xy} and $d_{x^2-y^2}$ orbitals), let \hat{O} be any operator in the D_{3h} symmetry group. Because the Hamiltonian of a TMD monolayer has a D_{3h} point-group symmetry, it must commute with \hat{O} , i.e. $[\hat{H},\hat{O}]=0$. But this may cause degeneracy between quantum states as follows: suppose $|\psi\rangle$ is an eigenstate of the TMD monolayer with eigenenergy ε , then

$$\hat{O}(\hat{H}|\psi\rangle) = \hat{O}(\varepsilon|\psi\rangle) = \varepsilon(\hat{O}|\psi\rangle) = \hat{H}(\hat{O}|\psi\rangle), \tag{2.5}$$

where the latter expression is allowed due to the fact that $[\hat{H}, \hat{O}] = 0$. One can see from this expression that if $|\psi\rangle$ is an eigenstate, then $\hat{O}|\psi\rangle$ is an eigenstate as well and it has the same eigenenergy as $|\psi\rangle$.

This can also be applied to the d_{xy} and $d_{x^2-y^2}$ orbitals. First, suppose that $|d_{xy}\rangle$ is an eigenstate of the

Hamiltonian with eigenenergy ε_2 . Applying the operator \hat{M}_1 to this state gives

$$\hat{M}_{1} \left| d_{xy} \right\rangle = i \left(\hat{M}_{1} \left| Y_{2}^{-2} \right\rangle - \hat{M}_{1} \left| Y_{2}^{2} \right\rangle \right) = i \left(\exp(-2\pi i/3) \left| Y_{2}^{2} \right\rangle - \exp(2\pi i/3) \left| Y_{2}^{-2} \right\rangle \right)
= \frac{1}{2} \left[\sqrt{3} \left(\left| Y_{2}^{-2} \right\rangle + \left| Y_{2}^{2} \right\rangle \right) + i \left(\left| Y_{2}^{-2} \right\rangle - \left| Y_{2}^{2} \right\rangle \right) \right] = \frac{1}{2} \left(\sqrt{3} \left| d_{x^{2} - y^{2}} \right\rangle + \left| d_{xy} \right\rangle \right).$$
(2.6)

To evaluate $\hat{M}_1 | Y_2^{\pm 2} \rangle$, note that $| Y_2^{\pm 2} \rangle \propto \exp(\pm 2i\phi)$ and that $\hat{M}_1 : \phi \to \pi/3 - \phi$, so that indeed $\hat{M}_1 | Y_2^{\pm 2} \rangle = \exp(\pm 2\pi i/3) | Y_2^{\mp 2} \rangle$. From what has been shown earlier in eq. (2.5), the state $\hat{M}_1 | d_{xy} \rangle$ also has to be an eigenstate with eigenenergy ε_2 . Because $| d_{xy} \rangle$ and $\hat{M}_1 | d_{xy} \rangle$ are degenerate states, any linear combination of these two states is also an eigenstate with eigenenergy ε_2 . But this means that

$$\frac{1}{\sqrt{3}} \left(2\hat{M}_1 \left| d_{xy} \right\rangle - \left| d_{xy} \right\rangle \right) = \left| d_{x^2 - y^2} \right\rangle \tag{2.7}$$

is also an eigenstate with eigenenergy ε_2 , which completes the proof that the d_{xy} and $d_{x^2-y^2}$ orbitals have to be degenerate. Note that a different symmetry operation could have been chosen, such as \hat{C}_3 , as long as the operation is in D_{3h} and results in a linear combination of d_{xy} and $d_{x^2-y^2}$ orbitals. Also note that the d_{z^2} orbital is not degenerate with the d_{xy} and $d_{x^2-y^2}$ orbitals, as there is no operation in D_{3h} that transforms a d_{xy} or $d_{x^2-y^2}$ into a superposition with a d_{z^2} orbital.

2.1.2 Hopping integrals

The hopping integrals considered by Liu et al. are all nearest neighbors (NN), second nearest neighbors (SNN), or third nearest neighbors (TNN). For simplicity, these overlaps are defined as

$$t_{ij} = \left\langle \phi_i(\mathbf{r}) \middle| \hat{H} \middle| \phi_j(\mathbf{r} - \mathbf{a}_1) \right\rangle, \tag{2.8}$$

$$r_{ij} = \left\langle \phi_i(\mathbf{r}) \middle| \hat{H} \middle| \phi_j(\mathbf{r} - 2\mathbf{a}_1 + \mathbf{a}_2) \right\rangle, \tag{2.9}$$

$$u_{ij} = \left\langle \phi_i(\mathbf{r}) \middle| \hat{H} \middle| \phi_j(\mathbf{r} - 2\mathbf{a}_1) \right\rangle, \tag{2.10}$$

where $|\phi_0\rangle=|d_{z^2}\rangle$, $|\phi_1\rangle=|d_{xy}\rangle$, and $|\phi_2\rangle=|d_{x^2-y^2}\rangle$, and these definitions will also be used in the remainder of this section about the three-band model. These parameters only define the NN, SNN and TNN hopping integrals for one specific direction. The main question remains what the hopping integrals in the other directions are. It turns out that these depend on the hopping integrals defined in eqs. (2.8) to (2.10) due to the D_{3h} point-group symmetry of the Hamiltonian. The case for t_{00} is simple, all NN hoppings should have the same energy due to the circular symmetry of the d_{z^2} orbital (see also fig. 2.1a). The same applies for the SNN hoppings (r_{00}) , or TNN hoppings (u_{00}) as only d_{z^2} orbitals are involved. All the other hopping integrals, however, involve d_{xy} and/or $d_{x^2-y^2}$ orbitals and from their plots (figs. 2.1b and 2.1c), it is clear that these integrals may be different for different NN, SNN or TNN. There are too many hopping integrals to work them all out, so only some examples are covered to give an idea how these integrals can be calculated. The results of all the other hopping integrals will be tabulated in tables 2.1 and 2.2. It is also worth to mention that once all the NN hopping integrals are found, all the TNN hopping integrals can easily found by analogy: one simply has to replace t by u, \mathbf{a}_1 by $2\mathbf{a}_1$, and \mathbf{a}_2 by $2\mathbf{a}_2$.

Table 2.1: Overview of all NN hopping integrals in terms of the expressions in eqs. (2.8) to (2.10). Note that TNN hopping integrals can be found by replacing t with u, \mathbf{a}_1 with $2\mathbf{a}_1$, and \mathbf{a}_2 with $2\mathbf{a}_2$.

| | neighbor positions | | |
|-------------------------------|--------------------|--|---|
| hopping orbitals | $\pm \mathbf{a}_1$ | $\pm a_2$ | $\pm(\mathbf{a}_2-\mathbf{a}_1)$ |
| $d_{z^2} \to d_{z^2}$ | t_{00} | t_{00} | t_{00} |
| $d_{z^2} \rightarrow d_{xy}$ | t_{01} | $\frac{\sqrt{3}t_{02}\pm t_{01}}{2}$ | $-\frac{\sqrt{3}t_{02}\pm t_{01}}{2}$ |
| $d_{z^2} \to d_{x^2 - y^2}$ | t_{02} | $\frac{\pm\sqrt{3}t_{01}-t_{02}}{2}$ | $\frac{\pm\sqrt{3}t_{01}-t_{02}}{2}$ |
| $d_{xy} \to d_{xy}$ | t_{11} | $\frac{3t_{22}+t_{11}}{4}$ | $\frac{3t_{22}+t_{11}}{4}$ |
| $d_{xy} \to d_{x^2 - y^2}$ | t_{12} | $\frac{\sqrt{3}}{4}(t_{11} - t_{22}) \mp t_{12}$ | $\frac{\sqrt{3}}{4}(t_{22}-t_{11})\pm t_{12}$ |
| $d_{x^2-y^2} \to d_{x^2-y^2}$ | t ₂₂ | $\frac{3t_{11}+t_{22}}{4}$ | $\frac{3t_{11}+t_{22}}{4}$ |

¹The normalization factor $\frac{1}{\sqrt{2}}$ of the d_{xy} orbital for convenience during the calculation has been omitted for convenience.

Table 2.2: Overview of all SNN hopping integrals in terms of the expressions in eqs. (2.8) to (2.10). The hopping integrals in the opposite directions are the same except that r_{01} should be replaced by r_{10} .

| | neighbor positions | | | |
|----------------------------------|--|--|--|--|
| hopping orbitals | $2a_1 - a_2$ | $2a_2 - a_1$ | $-a_1 - a_2$ | |
| $d_{z^2} \rightarrow d_{z^2}$ | r_{00} | r_{00} | r_{00} | |
| $d_{z^2} \rightarrow d_{xy}$ | r_{01} | 0 | $-r_{01}$ | |
| $d_{z^2} \to d_{x^2 - y^2}$ | $-r_{01}/\sqrt{3}$ | $\frac{2r_{01}}{\sqrt{3}}$ | $-\frac{r_{01}}{\sqrt{3}}$ | |
| $d_{xy} \rightarrow d_{xy}$ | r_{11} | $\frac{3r_{22}+r_{11}}{4}+\frac{1}{2}\sqrt{3}r_{12}$ | $\frac{3r_{22}+r_{11}}{4}-\frac{1}{2}\sqrt{3}r_{12}$ | |
| $d_{xy} \rightarrow d_{x^2-y^2}$ | r_{12} | 0 | $-r_{12}$ | |
| $d_{x^2-y^2} \to d_{x^2-y^2}$ | $r_{22} = r_{11} + \frac{2r_{12}}{\sqrt{3}}$ | $\frac{3r_{11}+r_{22}}{4}-\frac{1}{2}\sqrt{3}r_{12}$ | $\frac{3r_{11}+r_{22}}{4}+\frac{1}{2}\sqrt{3}r_{12}$ | |

In this section, the hopping between two orbitals with a relative displacement a is defined as

$$h_{ij}(\mathbf{a}) = \left\langle \phi_i(\mathbf{r}) \middle| \hat{H} \middle| \phi_j(\mathbf{r} - \mathbf{a}) \right\rangle. \tag{2.11}$$

The first example that will be worked out is the hopping integral $h_{12}(\mathbf{a}_2)$. In order to do that, one can exploit the D_{3h} point-group symmetry of the Hamiltonian. Suppose that \hat{O} is a symmetry operation in D_{3h} , then the Hamiltonian can be rewritten as

$$\hat{H} = \hat{O}^{-1}\hat{O}\hat{H} = \hat{O}^{-1}\hat{H}\hat{O},\tag{2.12}$$

as $[\hat{H}, \hat{O}] = 0$. What can be seen from this expression is that one can always sandwich the Hamiltonian between a symmetry operator in D_{3h} and its inverse. By making a smart choice for \hat{O} , one can then express $h_{12}(\mathbf{a}_2)$ in terms of the hopping integrals given in eqs. (2.8) to (2.10). As the center of the $d_{x^2-y^2}$ orbital is at \mathbf{a}_2 while the center of the known hopping integrals are at \mathbf{a}_1 , it makes sense to choose $\hat{O} = \hat{M}_1$, so that the ket part of $h_{12}(\mathbf{a}_2)$ becomes

$$\hat{M}_1 \left| d_{x^2 - y^2}(\mathbf{r} - \mathbf{a}_2) \right\rangle = \frac{1}{2} \left(\sqrt{3} \left| d_{xy}(\mathbf{r} - \mathbf{a}_1) \right\rangle - \left| d_{x^2 - y^2}(\mathbf{r} - \mathbf{a}_1) \right\rangle \right), \tag{2.13}$$

which can be derived in a similar way as the mirror operation on the d_{xy} orbital (see eq. (2.6)). Using the fact that a reflection operation is unitary and equals its inverse (i.e. $\hat{M}_1 = \hat{M}_1^{-1} = \hat{M}_1^{\dagger}$), the bra part of $h_{12}(\mathbf{a}_2)$ evaluates to

$$\left[\hat{M}_{1}\left|d_{xy}(\mathbf{r})\right\rangle\right]^{\dagger} = \frac{1}{2}\left(\left\langle d_{x^{2}-y^{2}}(\mathbf{r})\right|\sqrt{3} + \left\langle d_{xy}(\mathbf{r})\right|\right). \tag{2.14}$$

Putting together then gives

$$h_{12}(\mathbf{a}_2) = \frac{\sqrt{3}}{4}(t_{11} - t_{22}) + \frac{3t_{21} - t_{12}}{4},\tag{2.15}$$

where $t_{21} = \left\langle d_{x^2-y^2}(\mathbf{r}) \middle| \hat{H} \middle| d_{xy}(\mathbf{r} - \mathbf{a}_1) \right\rangle$ still needs to be evaluated as it turns out to be a dependent hopping integral. To derive an expression for t_{21} , first make use of the \hat{M}_2 symmetry of the Hamiltonian so that

$$t_{21} = \left\langle d_{x^2 - y^2}(\mathbf{r}) \middle| \hat{M}_2 \hat{H} \hat{M}_2 \middle| d_{xy}(\mathbf{r} - \mathbf{a}_1) \right\rangle = -\left\langle d_{x^2 - y^2}(\mathbf{r}) \middle| \hat{H} \middle| d_{xy}(\mathbf{r} + \mathbf{a}_1) \right\rangle. \tag{2.16}$$

Next, the translational symmetry of the Hamiltonian can be used and the corresponding operator is defined as $\hat{T}_{\mathbf{a}} | \psi(\mathbf{r}) \rangle = | \psi(\mathbf{r} + \mathbf{a}) \rangle$. As the inverse of $\hat{T}_{\mathbf{a}}$ is simply $\hat{T}_{-\mathbf{a}}$ and the lattice is periodic in \mathbf{a}_1 , t_{21} can be rewritten as

$$t_{21} = -\left\langle d_{x^2 - y^2}(\mathbf{r}) \middle| \hat{T}_{\mathbf{a}_1} \hat{H} \hat{T}_{-\mathbf{a}_1} \middle| d_{xy}(\mathbf{r} + \mathbf{a}_1) \right\rangle = -\left\langle d_{x^2 - y^2}(\mathbf{r} - \mathbf{a}_1) \middle| \hat{H} \middle| d_{xy}(\mathbf{r}) \right\rangle. \tag{2.17}$$

But from this, the complex conjugate of t_{12} can be recognized, and since all the hopping integrals in Liu et al. are real, one will obtain $t_{21} = -t_{12}$, so that the final expression will become

$$h_{12}(\mathbf{a}_2) = \frac{\sqrt{3}}{4}(t_{11} - t_{22}) - t_{12}. \tag{2.18}$$

An analysis similar to that of $h_{12}(\mathbf{a}_2)$ can be done for $h_{12}(\mathbf{a}_2 - \mathbf{a}_1)$, but instead of the \hat{M}_1 operation, the \hat{C}_3^{-1} operation need to be used instead. The bra and ket terms will thus become

$$\hat{C}_{3}^{-1} \left| d_{x^{2}-y^{2}}(\mathbf{r} - \mathbf{a}_{2} + \mathbf{a}_{1}) \right\rangle = \frac{1}{2} \left(\sqrt{3} \left| d_{xy}(\mathbf{r} - \mathbf{a}_{1}) \right\rangle - \left| d_{x^{2}-y^{2}}(\mathbf{r} - \mathbf{a}_{1}) \right\rangle \right), \tag{2.19}$$

$$\left\langle d_{xy}(\mathbf{r}) \middle| \hat{C}_3 = -\frac{1}{2} \left(\left\langle d_{x^2 - y^2}(\mathbf{r}) \middle| \sqrt{3} + \left\langle d_{xy}(\mathbf{r}) \middle| \right), \right.$$
 (2.20)

so that

$$h_{12}(\mathbf{a}_2 - \mathbf{a}_1) = \frac{\sqrt{3}}{4}(t_{22} - t_{11}) + t_{12}. \tag{2.21}$$

The hopping integrals to the other nearest neighbors can also be found with this analysis by using the appropriate symmetry operations. However, by doing a similar derivation as the one for t_{21} , it turns out that the hopping integral in a given direction is the same as the one in the opposite direction except for a minus sign in front of t_{01} and t_{12} .

The calculation of the SNN hoppings is a bit different from the calculation of the NN and the TNN hoppings. In case of NN hoppings, t_{01} and t_{10} (idem for t_{02} and t_{20}) are dependent hopping integrals due to the \hat{M}_2 symmetry operation, while t_{01} and t_{02} (idem for t_{10} and t_{20}) are independent. For SNN hoppings (where t is replaced by r), however, this is the other way around and the dependence between t_{01} and t_{02} (and between t_{10} and t_{20}) can be found by means of the \hat{M}_3 symmetry operation:

$$r_{02} = -\frac{r_{01}}{\sqrt{3}},\tag{2.22}$$

$$r_{20} = -\frac{r_{10}}{\sqrt{3}}. (2.23)$$

It should also be remarked that in Liu et al. the parameter r_2 should be the value for r_{10} in order to reproduce their results². The reason why a hopping integral r_{22} is 'missing' in Liu et al. (compare the NN and TNN case) is because it is not an independent parameter. In order to see that, consider the hopping integrals r_{12} and r_{21} . Due to the \hat{M}_3 symmetry of the lattice,

$$r_{12} = \frac{\sqrt{3}}{4}(r_{22} - r_{11}) + \frac{3r_{21} - r_{12}}{4},\tag{2.24}$$

$$r_{21} = \frac{\sqrt{3}}{4}(r_{22} - r_{11}) + \frac{3r_{12} - r_{21}}{4}.$$
 (2.25)

It can easily be verified (by subtracting eq. (2.25) from eq. (2.24)) that the only way that both equations can hold, is when $r_{12} = r_{21}$. This, however, also means that either r_{22} or r_{11} must be a dependent hopping integral. In Liu et al. this is chosen to be r_{22} and after some calculation, this hopping integral is given by

$$r_{22} = r_{11} + \frac{2r_{12}}{\sqrt{3}}. (2.26)$$

2.1.3 Spin-orbit interaction

One of interactions in the solid that will be very important later in the thesis is the spin-orbit interaction (abbreviated as SOI in the rest of this thesis). This can be described as an atomic $\hat{\mathbf{L}} \cdot \hat{\mathbf{S}}$ -like perturbation to the Hamiltonian. Implementing this in the three-band model in Kwant is not too difficult. Using the basis $\{|d_{z^2},\uparrow\rangle,|d_{xy},\uparrow\rangle,|d_{x^2-y^2},\uparrow\rangle,|d_{z^2},\downarrow\rangle,|d_{xy},\downarrow\rangle,|d_{xy},\downarrow\rangle,|d_{xy},\downarrow\rangle,|d_{xy},\downarrow\rangle\}$, the onsite Hamiltonian need to be replaced by

$$\hat{H}_{onsite} = \hat{I}_2 \otimes \hat{H}_0 + \lambda \left(\hat{S}_x \otimes \hat{L}_x + \hat{S}_y \otimes \hat{L}_y + \hat{S}_z \otimes \hat{L}_z \right), \tag{2.27}$$

where \hat{I}_2 is a 2 × 2 identity matrix and \hat{H}_0 is the unperturbed onsite Hamiltonian given by eq. (2.4). Next step is to evaluate \hat{L}_x , \hat{L}_y , and \hat{L}_z operators for the given basis. Note that the cubic harmonics can be expressed in terms of the spherical harmonics given in eqs. (2.1) to (2.3), which are eigenvectors of \hat{L}_z . After some calculation, it can be found that $\hat{L}_x = \hat{L}_y = 0$ and that³

$$\hat{L}_z = \begin{pmatrix} 0 & 0 & 0 \\ 0 & 0 & 2i \\ 0 & -2i & 0 \end{pmatrix},\tag{2.28}$$

so that eq. (2.27) can be simplified to

$$\hat{H}_{onsite} = \begin{pmatrix} \hat{H}_0 + \frac{\lambda}{2} \hat{L}_z & 0\\ 0 & \hat{H}_0 - \frac{\lambda}{2} \hat{L}_z \end{pmatrix}. \tag{2.29}$$

Note that the Hamiltonian is block diagonal with respect to the spin Hilbert space, which makes the spin in the *z*-direction good quantum numbers.

²The statement that $r_2 = r_{20}$ in Liu et al.'s erratum [22] is therefore wrong as well.

 $^{^3}$ The \hbar is omitted for convenience as it can also be put into the λ .

2.1.4 Results and discussion

The resulting band structure of the three-band model for MoS_2 is given in fig. 2.3. To this end, the fitted parameters of the generalized-gradient approximation (GGA) for MoS_2 from Liu et al. are used. According to Liu et al., the strength of the $SOI(\lambda)$ is 0.073 eV for MoS_2 . It can be seen that the three-band model implemented in Kwant (fig. 2.3a) visually agrees with the band structure in Liu et al. Furthermore, the splitting along a trajectory through a +K point is opposite to that through a -K point. This confirms the statement in the introduction that TMD monolayers have Ising SOI. The band structure with SOI of the 3-band model has two remarkable properties: (1) there is no splitting in any band along the Γ -M trajectory, and (2) there is no splitting in the conduction band at the $\pm K$ point. The former can be explained by means of symmetry arguments, but the latter is not in agreement with expectation [23, 24].

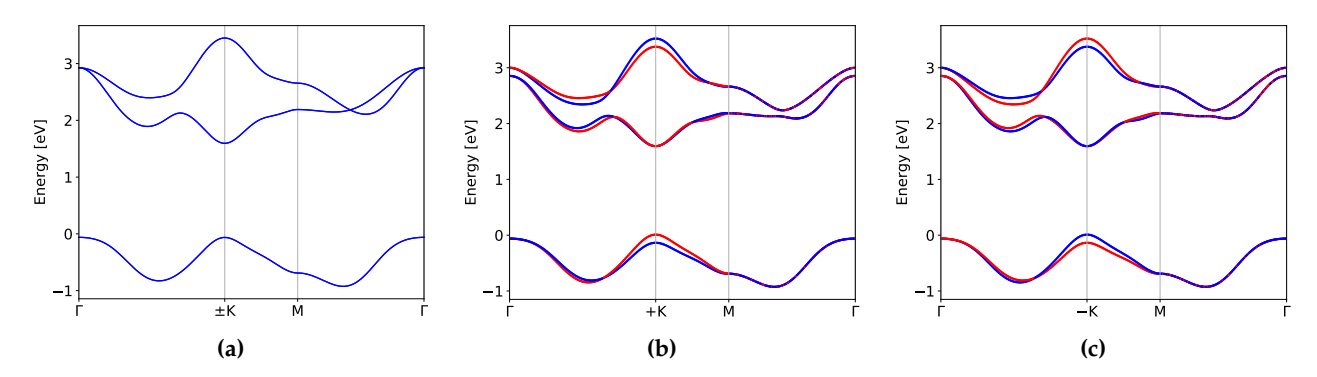


Figure 2.3: The 3-band structure of MoS_2 from Liu et al.'s paper: (a) no SOI; (b and C) SOI interaction with the trajectory through a +K point (b) or -K point (c). The red lines indicate spin-up bands, the blue lines indicate spin-down bands.

To explain why there is no splitting along the Γ -M trajectory, recall that if $[\hat{H},\hat{O}]=0$ and $|\psi\rangle$ is an eigenstate of \hat{H} , then $\hat{O}|\psi\rangle$ is also an eigenstate with same eigenenergy as $|\psi\rangle$. For the M and Γ point, the time reversal operator $\hat{\mathcal{T}}$ can be used. It should be noted that $\hat{\mathcal{T}}$ is an antilinear and antiunitary operator, which requires caution as computation with such operators is a bit different than with unitary and linear operators. Both the tight-binding Hamiltonian $\hat{H}(\mathbf{k})$ and the spin-orbit Hamiltonian are symmetric under time reversal, i.e. $[\hat{H},\hat{\mathcal{T}}]=0$. This also implies that for the tight-binding Hamiltonian

$$\hat{H}(\mathbf{k}) = \hat{\mathcal{T}}^{-1}\hat{H}(\mathbf{k})\hat{\mathcal{T}} = \hat{H}^*(-\mathbf{k}). \tag{2.30}$$

Furthermore, the time reversal operator flips crystal momentum and spin so that

$$\hat{\mathcal{T}}|\psi\rangle = \hat{\mathcal{T}}|\mathbf{k},\uparrow\downarrow\rangle = \exp(i\varphi)|-\mathbf{k},\downarrow\uparrow\rangle, \qquad (2.31)$$

where φ is some phase. The states $|\psi\rangle$ and $\hat{\mathcal{T}}|\psi\rangle$ are not only degenerate, but also always orthogonal due to fact that the spin is a half-integer. All states are therefore at least twofold degenerate and this is also known as Kramer's degeneracy theorem. From eq. (2.31), it is clear that if \mathbf{k} and $-\mathbf{k}$ represent equivalent crystal momenta, then there will be no spin splitting at crystal momentum \mathbf{k} . It is then straightforward to see that the Γ and M points have no spin splitting, namely if \mathbf{k} is such a point, then $-\mathbf{k}$ is such a point as well. However, in order to explain that there is no splitting along the Γ-M trajectory, one need the mirror symmetry along that trajectory. If \mathbf{k} is at the trajectory, then $\hat{M}_i | \mathbf{k}, \uparrow \downarrow \rangle = \exp(i\varphi) | \mathbf{k}, \downarrow \uparrow \rangle$ and thus there is no spin-splitting along the Γ-M trajectory due to the mirror symmetry.

To explain why there is no splitting of the conduction band in the three-band model at the $\pm K$ point, note that an eigenstate at point ${\bf k}$ in reciprocal space can be expressed as

$$|\psi(\mathbf{k}),\uparrow\downarrow\rangle = \alpha(\mathbf{k}) \left| Y_2^{-2},\uparrow\downarrow \right\rangle + \beta(\mathbf{k}) \left| Y_2^{0},\uparrow\downarrow \right\rangle + \gamma(\mathbf{k}) \left| Y_2^{2},\uparrow\downarrow \right\rangle. \tag{2.32}$$

For such states, the first order energies of the SOI is given by

$$\langle \psi(\mathbf{k}), \uparrow \downarrow | \hat{L}_z \hat{S}_z | \psi(\mathbf{k}), \uparrow \downarrow \rangle = \pm \left(|\gamma(\mathbf{k})|^2 - |\alpha(\mathbf{k})|^2 \right). \tag{2.33}$$

It is clear from this expression that there will be no splitting if $|\gamma(\mathbf{k})| = |\alpha(\mathbf{k})|$, which is for example the case for the d_{z^2} , d_{xy} and $d_{x^2-y^2}$ orbitals. From fig. 2 in Liu et al.'s paper, it can be seen that the eigenstate of the conduction band at the $\pm K$ point is $|d_{z^2}\rangle$, and this will not be split by SOI. It can also be derived analytically using eqs. (15) to (18) from Liu et al. that $\langle d_{z^2}|\hat{H}(\mathbf{k})|d_{xy}\rangle = \langle d_{z^2}|\hat{H}(\mathbf{k})|d_{x^2-y^2}\rangle = 0$ if \mathbf{k} is a $\pm K$ point. This means that the $|d_{z^2}\rangle$ state is decoupled from the other orbitals and thus $|d_{z^2}\rangle$ is one of the eigenstates at the

 \pm K point. As mentioned earlier, however, there is some splitting expected in the conduction band and this will only be visible when the p-orbitals of the chalcogen atoms are included, which will be shown later in the 11-band model. This splitting at the conduction band will also be relevant later in this thesis, as this is needed to describe the vanishing SOI in the conduction band.

2.2 11-band tight binding model

As discussed in the previous section, the three-band model does not reproduce the expected SOI splitting in the conduction band at the $\pm K$ point. Therefore, the more accurate 11-band model of Fang et al.[25] will be used instead. It has already been explained in detail how to calculate dependent hopping integrals using symmetries in section 2.1, so it will not be done again in this section.

2.2.1 Orbitals and hopping integrals

The orbitals that are included in the 11-band model are the 5 d-orbitals of the transition metal and the 3 p-orbitals of both the top and the bottom chalcogen atoms (remember fig. 1.1a in the introduction). The 5 d-orbitals are d_{z^2} , d_{xy} , $d_{x^2-y^2}$, d_{xz} and d_{yz} , and the last two orbitals are, just like the other 3 discussed in the three-band model, cubic harmonics that are related to the spherical harmonics according to

$$|d_{xz}\rangle = \frac{1}{\sqrt{2}} \left(\left| Y_2^{-1} \right\rangle - \left| Y_2^{1} \right\rangle \right),\tag{2.34}$$

$$\left| d_{yz} \right\rangle = \frac{i}{\sqrt{2}} \left(\left| Y_2^{-1} \right\rangle + \left| Y_2^{1} \right\rangle \right). \tag{2.35}$$

The two chalcogen atoms each have a p_x , p_y and p_z orbital that are related to the spherical harmonics according to

$$|p_x\rangle = \frac{1}{\sqrt{2}} \left(\left| Y_1^{-1} \right\rangle - \left| Y_1^{1} \right\rangle \right),\tag{2.36}$$

$$\left| p_y \right\rangle = \frac{i}{\sqrt{2}} \left(\left| Y_1^{-1} \right\rangle + \left| Y_1^{1} \right\rangle \right), \tag{2.37}$$

$$|p_z\rangle = |Y_1^0\rangle. \tag{2.38}$$

It is convenient to hybridize the p orbitals of the top and bottom layer as follows:

$$|p_{x}^{o}\rangle = \frac{1}{\sqrt{2}}(|p_{x}^{A}\rangle - |p_{x}^{B}\rangle), \quad |p_{y}^{o}\rangle = \frac{1}{\sqrt{2}}(|p_{y}^{A}\rangle - |p_{y}^{B}\rangle), \quad |p_{z}^{o}\rangle = \frac{1}{\sqrt{2}}(|p_{z}^{A}\rangle + |p_{z}^{B}\rangle), \quad (2.39)$$

$$|p_x^e\rangle = \frac{1}{\sqrt{2}} \left(\left| p_x^A \right\rangle + \left| p_x^B \right\rangle \right), \quad \left| p_y^e \right\rangle = \frac{1}{\sqrt{2}} \left(\left| p_y^A \right\rangle + \left| p_y^B \right\rangle \right), \quad \left| p_z^e \right\rangle = \frac{1}{\sqrt{2}} \left(\left| p_z^A \right\rangle - \left| p_z^B \right\rangle \right), \tag{2.40}$$

where A and B indicate the top and bottom layer respectively. These hybridized p orbitals are eigenstates of the mirror operation in the xy-plane \hat{M}_{xy} , which will be useful later on. The two chalcogen atoms in the top and bottom layer can effectively be replaced with one atom in the transition metal layer, and these effective atoms have these 6 hybridized orbitals.

The 11-band model takes the following hoppings into account:

- All nearest neighbor hoppings between two transition metal atoms (NN M-M).
- All nearest neighbor hoppings between two chalcogen atoms (NN X-X).
- All nearest neighbor hoppings between a chalcogen atom and a transition metal atom (NN X-M).
- Some second nearest neighbor hoppings between a chalcogen atom and a transition metal atom (SNN X-M). This is done for improved accuracy.

The number of possible hopping directions times the number of orbitals in the model gives a lot of parameters. Fortunately, most of these parameters can be eliminated by considering the \hat{M}_{xy} symmetry of the Hamiltonian. To this end, one has to check whether the orbitals correspond to an eigenvalue of 1 or -1 under the \hat{M}_{xy} operation. An eigenvalue of 1 means that the orbital is even under \hat{M}_{xy} while an eigenvalue of -1 means that the orbital is odd under \hat{M}_{xy} . It can be found out that the d_{z^2} , d_{xy} , $d_{x^2-y^2}$, p_x^e , p_y^e , and p_z^e orbitals are even under \hat{M}_{xy} , while the d_{xz} , d_{yz} , p_x^o , p_y^o , and p_z^o orbitals are odd under \hat{M}_{xy} . The key point is that there is no hopping between an even and odd orbital. In order to see this, let $|\phi_i(\mathbf{r})\rangle$ and $|\phi_i(\mathbf{r}-\mathbf{a})\rangle$ be an even and odd orbital

respectively. Note that the hopping direction **a** lies in the xy-plane so that this will not be affected when \hat{M}_{xy} is applied. However, this means that

$$\langle \phi_i(\mathbf{r}) | \hat{H} | \phi_j(\mathbf{r} - \mathbf{a}) \rangle = \langle \phi_i(\mathbf{r}) | \hat{M}_{xy} \hat{H} \hat{M}_{xy} | \phi_j(\mathbf{r} - \mathbf{a}) \rangle = -\langle \phi_i(\mathbf{r}) | \hat{H} | \phi_j(\mathbf{r} - \mathbf{a}) \rangle, \tag{2.41}$$

and the only way this can hold is when the hopping integral is 0. Therefore, only hopping integrals between two even orbitals or two odd orbitals have to be considered, and this reduces the amount of parameters significantly.

2.2.2 Spin-orbit interaction

Just like in the three-band model, an $\hat{\mathbf{L}} \cdot \hat{\mathbf{S}}$ -like, momentum-independent SOI is used. It should be kept in mind, however, that the strength of the interaction at the transition metal is different than at the chalcogen atoms. The spin orbit Hamiltonian can thus be expressed like

$$\hat{H}_{SOI} = \left(\lambda_M \hat{\mathbf{L}}_M + \lambda_X \hat{\mathbf{L}}_X^A + \lambda_X \hat{\mathbf{L}}_X^B\right) \cdot \hat{\mathbf{S}}.$$
 (2.42)

$$\hat{H} = \begin{pmatrix} \Delta \varepsilon(\mathbf{k})/2 + t_3(\mathbf{k})/2 & 0 & 0 & t_1 \\ 0 & -\Delta \varepsilon(\mathbf{k})/2 + t_4(\mathbf{k})/2 & t_2^* & 0 \\ 0 & t_2 & \Delta \varepsilon(\mathbf{k})/2 - t_3(\mathbf{k})/2 & 0 \\ t_1^* & 0 & 0 & -\Delta \varepsilon(\mathbf{k})/2 - t_4(\mathbf{k})/2 \end{pmatrix}.$$
(2.43)

From this expression, it can be concluded that the z component of the spin is approximately a good quantum number if $|t_1(\mathbf{k})|$, $|t_2(\mathbf{k})| \ll |\Delta \varepsilon(\mathbf{k}) \pm t_{3,4}(\mathbf{k})|$. This is the case for the most part of the band structure as $\Delta \varepsilon(\mathbf{k})$ can be in the order of multiple eV, while the strength of the SOI is only in order of 50–80 meV for MoS₂. The only way mixing of spin-up and spin-down may occur, is when even and odd bands would cross each other if there would be no SOI. In fact, the spin orbit-interaction will cause small anticrossings between such bands and at these anticrossings, mixing of spin-up and spin-down will occur.

2.2.3 Results and discussion

The results of the 11-band model for MoS_2 are displayed in fig. 2.4. The used fit parameters are based on the DFT calculations, and can be found in table VII of Fang et al.'s paper. The strength of the SOI can also be found and is given in table VIII. The resulting band structure in fig. 2.4a is calculated with Kwant, and is in agreement with the one in Fang et al.'s paper (fig. 3). The band structure with SOI is displayed in fig. 2.4b. As discussed in section 2.2.2, mixing of spin-up and spin-down states is not visible in the figure, except where an even and odd orbital would cross each other (see fig. 2.4c).

In the three-band model, it has been shown that there was no splitting in the conduction band at the +K point due to the fact that the d_{z^2} orbital is decoupled from the d_{xy} and $d_{x^2-y^2}$ orbitals. In the 11-band model, these is a small splitting of the conduction band (see fig. 2.4d). In first order, this splitting cannot be caused by the other two d orbitals (d_{xz} and d_{yz}), as these states have to be decoupled from the d_{z^2} orbital due to the \hat{M}_{xy} symmetry. Thus, the origin of the splitting (in first order) have to be the p orbitals of the chalcogen atoms. In table IV of Fang et al.'s paper, it indeed turns out that the eigenstate of the lowest conduction band has a small contribution from the p orbitals of the chalcogen atoms:

$$|\psi_c\rangle \approx 0.9154i |d_{z^2}\rangle + 0.4026 |p_{-1}^e\rangle,$$
 (2.44)

 $^{^{4}}$ It is also worth to mention that this is also the reason why the three-band model did not have an x and y-component of angular momentum.

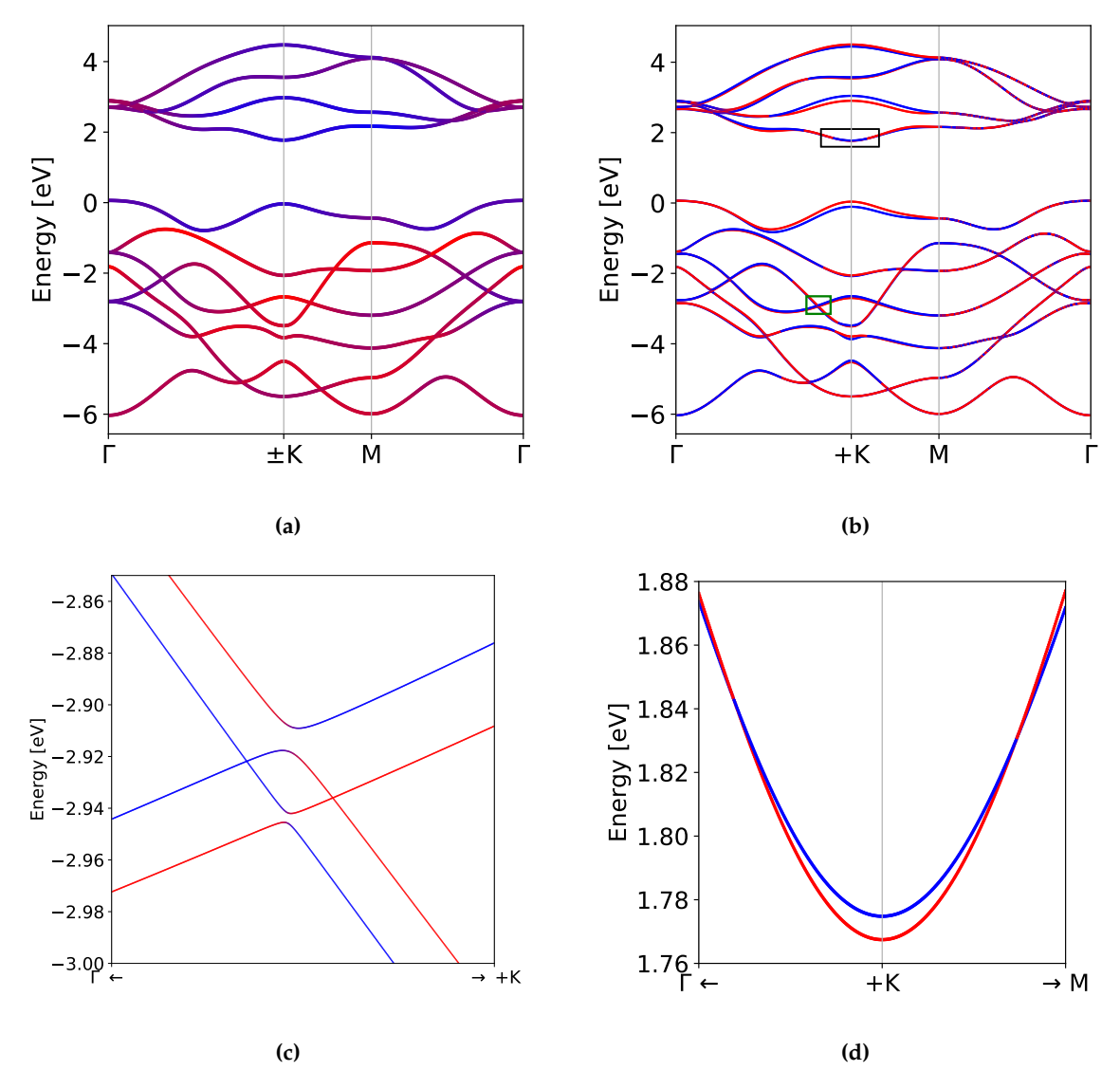


Figure 2.4: The 11-band structure of MoS₂ from Fang et al.'s paper. The used fit parameters are from the DFT method. (a) no SOI. Red-colored bands have p orbitals as eigenstate, whereas blue-colored bands have d orbitals as eigenstate. Purple-colored bands have a mix of p and d orbitals as eigenstate; (b) SOI with trajectory through a +K point. The red lines indicate spin-up bands, the blue lines indicate spin-down bands; (c) zoom of an anticrossing of two filled bands, indicated with the green box in (b); (d) zoom of the conduction band at the +K point, indicated with a black rectangle in (b).

where $\left|p_{-1}^{e}\right\rangle = \left(\left|p_{x}^{e}\right\rangle - i\left|p_{y}^{e}\right\rangle\right)/\sqrt{2}$. From this expression, the splitting of the spin-up and spin-down band can be approximated with first-order perturbation theory:

$$\varepsilon_{\uparrow} - \varepsilon_{\downarrow} \approx \lambda_X (0.4026)^2 \left(\left\langle p_{-1}^e, \uparrow \middle| \hat{\mathbf{L}} \cdot \hat{\mathbf{S}} \middle| p_{-1}^e, \uparrow \right\rangle - \left\langle p_{-1}^e, \downarrow \middle| \hat{\mathbf{L}} \cdot \hat{\mathbf{S}} \middle| p_{-1}^e, \downarrow \right\rangle \right) \approx -0.009 \,\text{eV},$$
 (2.45)

which is a small splitting compared to that of the valence band $\varepsilon_{\uparrow} - \varepsilon_{\downarrow} \approx 0.15\,\text{eV}$ (see also figure 4 of Fang et al.).

2.3 $\mathbf{k} \cdot \mathbf{p}$ method around the $\pm \mathbf{K}$ point

An interesting feature of the spin splitting of the conduction band in MoS_2 is that the spin-up and spin-down band cross each other near the $\pm K$ point. Such a crossing does not always happen in all TMD monolayers. TMD monolayers with molybdenum as transition metal usually have this crossing, but monolayers with tungsten do not [26]. This crossing, however, is very important later on, as these are the source of nodal topological superconductivity which will be explained in the next chapter. It is useful later on to have a simple, but accurate expression of the conduction band near the $\pm K$ point, and this can be done by deriving a $\mathbf{k} \cdot \mathbf{p}$ model.

2.3.1 $k \cdot p$ model

In order to set up a $\mathbf{k} \cdot \mathbf{p}$ model around a symmetry point, a set of eigenstates at that point in reciprocal space is required. Most models only pick (approximate) eigenstates of the lowest conduction band and highest valence band, and this is also sufficient in this case. According to the three-band model (section 2.1), the eigenstates of the conduction and valence band at the ηK point are given by

$$|\psi_{ch}\rangle = |d_{z^2}\rangle \,, \tag{2.46}$$

$$\left|\psi_{vb}^{\eta}\right\rangle = \frac{1}{\sqrt{2}} \left(\left|d_{x^2 - y^2}\right\rangle + i\eta \left|d_{xy}\right\rangle\right),\tag{2.47}$$

respectively, where η represents either +1 or -1. Using the basis $\{|\psi_{cb}\rangle, |\psi_{vb}^{\eta}\rangle\}$, the most general form of the Hamiltonian is given by

$$\hat{H}_n = f_{L,n}(k_x, k_y)\hat{I} + f_{X,n}(k_x, k_y)\hat{X} + f_{Y,n}(k_x, k_y)\hat{Y} + f_{Z,n}(k_x, k_y)\hat{Z}, \tag{2.48}$$

where k_x , k_y represents the crystal momentum with respect to the η K point, \hat{l} is the identity matrix, and \hat{X} , \hat{Y} , and \hat{Z} are the Pauli matrices. The identity matrix and the Pauli matrices namely form a basis for all 2×2 hermitian matrices. The $\mathbf{k} \cdot \mathbf{p}$ method approximates the Hamiltonian for small k_x , k_y by treating a deviation from the symmetry point as a perturbation⁵. $f_{i,\eta}(k_x,k_y)$ in eq. (2.48) can therefore be written out as a Taylor series. In this case, it is sufficient to go up to second order, which means that the most general form of $f_{i,\eta}(k_x,k_y)$ is given by

$$f_{i,\eta}(k_x, k_y) = a_0^i + a_{1,x}^i k_x + a_{1,y}^i k_y + a_{2,xx}^i k_x^2 + a_{2,yy}^i k_y^2 + a_{2,xy}^i k_x k_y, \tag{2.49}$$

which means that up to second order, the $\mathbf{k} \cdot \mathbf{p}$ Hamiltonian may be described by 24 parameters. However, a lot of these parameters will vanish or are related to each other when the symmetries of the Hamiltonian are considered. At the η K point, the reciprocal space of the TMD monolayer has a C_{3h} point-group symmetry (a subgroup of D_{3h}), which only contains the rotation operations and \hat{M}_{xy} . The rotation symmetries require that

$$\hat{H}_{\eta}(k_x, k_y) = \hat{C}_3^{\dagger} \hat{H}_{\eta} \left(\frac{-k_x - \sqrt{3}k_y}{2}, \frac{-\sqrt{3}k_x + k_y}{2} \right) \hat{C}_3. \tag{2.50}$$

Although the ηK point does not have a mirror symmetry and the time reversal symmetry, they do relate the $\mathbf{k} \cdot \mathbf{p}$ Hamiltonian at the ηK point with the one at the $-\eta K$ point. In particular, the yz-plane mirror operation \hat{M}_2 requires

$$\hat{M}_2 \hat{H}_\eta(k_x, k_y) \hat{M}_2 = \hat{H}_{-\eta}(-k_x, k_y). \tag{2.51}$$

Furthermore, the time reversal symmetry demands

$$\hat{\mathcal{T}}^{-1}\hat{H}_{\eta}(k_x, k_y)\hat{\mathcal{T}} = \hat{H}^*_{-\eta}(-k_x, -k_y). \tag{2.52}$$

In order to find out which parameters in eq. (2.49) vanish or are related to each other, it helps to look at the terms of the Taylor series in this equation separately, which will be done in the next series of paragraphs.

The zeroth order The most general form of the zeroth order $\mathbf{k} \cdot \mathbf{p}$ Hamiltonian is given by

$$\hat{H}_{\eta}^{(0)} = a_0^I \hat{I} + a_0^X \hat{X} + a_0^Y \hat{Y} + a_0^Z \hat{Z}. \tag{2.53}$$

As the $\mathbf{k} \cdot \mathbf{p}$ Hamiltonian has a C_{3h} point-group symmetry, the rotation operator \hat{C}_3 must commute with $\hat{H}_{\eta}^{(0)}$. This also means that the eigenstates of $\hat{H}_{\eta}^{(0)}$ are also eigenstates of \hat{C}_3 and the corresponding eigenvalues are given by

$$\hat{C}_3 |\psi_{ch}\rangle = |\psi_{ch}\rangle, \tag{2.54}$$

$$\hat{C}_3 \left| \psi_{vb}^{\eta} \right\rangle = \exp(2\pi \eta i/3) \left| \psi_{vb}^{\eta} \right\rangle. \tag{2.55}$$

 $^{^5}$ It's also nice to mention that this perturbation of the Hamiltonian actually has the form $\mathbf{k} \cdot \mathbf{p}$ (hence the name) where \mathbf{k} is the crystal momentum with respect to the symmetry point and \mathbf{p} the momentum operator.

from this, the effect of the rotation operator on the identity (trivial) and the Pauli matrices can be calculated, and are given by

$$\hat{C}_{3}^{\dagger}\hat{I}\hat{C}_{3} = \hat{I},\tag{2.56}$$

$$\hat{C}_{3}^{\dagger}\hat{X}\hat{C}_{3} = -\frac{1}{2}(\sqrt{3}\eta\hat{Y} + \hat{X}), \tag{2.57}$$

$$\hat{C}_{3}^{\dagger}\hat{Y}\hat{C}_{3} = \frac{1}{2}(\sqrt{3}\eta\hat{X} - \hat{Y}),\tag{2.58}$$

$$\hat{C}_3^{\dagger} \hat{Z} \hat{C}_3 = \hat{Z}. \tag{2.59}$$

Using eq. (2.50), it is clear that the \hat{I} and \hat{Z} component in the zeroth order expression remains invariant, while it requires for the \hat{X} and \hat{Y} component that

$$a_0^X = -\frac{1}{2}a_0^X + \frac{\sqrt{3}}{2}\eta a_0^Y, \tag{2.60}$$

$$a_0^Y = -\frac{1}{2}a_0^Y - \frac{\sqrt{3}}{2}\eta a_0^X. \tag{2.61}$$

Both of these equations can only hold if $a_0^X = a_0^Y = 0$. Thus, the C_{3h} point-group symmetry of the $\mathbf{k} \cdot \mathbf{p}$ Hamiltonian requires that the zeroth order expression does not have an \hat{X} and \hat{Y} component, but a_0^I and a_0^Z are free parameters. Using physical intuition, one can express the zeroth order $\mathbf{k} \cdot \mathbf{p}$ Hamiltonian as

$$\hat{H}_{\eta}^{(0)} = -\mu \hat{I} + \frac{E_g}{2} (\hat{I} + \hat{Z}), \tag{2.62}$$

where μ represents the chemical potential and E_g the band gap energy. It is convenient to set $\mu = 0$ as this term only shifts the eigenenergies of the system, and this will also be done in the remainder of this chapter.

The first order The most general form of the first order $\mathbf{k} \cdot \mathbf{p}$ Hamiltonian is given by

$$\hat{H}_{\eta}^{(1)} = \left(a_x^I k_x + a_y^I k_y \right) \hat{I} + \left(a_x^X k_x + a_y^X k_y \right) \hat{X} + \left(a_x^Y k_x + a_y^Y k_y \right) \hat{Y} + \left(a_x^Z k_x + a_y^Z k_y \right) \hat{Z}. \tag{2.63}$$

Using the rotational symmetry requirement given in eq. (2.50) and using the relations given in eqs. (2.56) to (2.59), the \hat{I} component is given by

$$a_x^I k_x + a_y^I k_y = \frac{1}{2} \left[-a_x^I \left(k_x + \sqrt{3} k_y \right) + a_y^I \left(\sqrt{3} k_x - k_y \right) \right]. \tag{2.64}$$

The same expression can be obtained for the \hat{Z} by replacing I by Z in the equation. The equation has to hold for all k_x , k_y and this requirement can only be satisfied if $a_x^I = a_y^I = a_x^Z = a_y^Z = 0$. Thus, the first order expression of the $\mathbf{k} \cdot \mathbf{p}$ Hamiltonian has no \hat{I} and \hat{Z} component. For the \hat{X} component, the following equations from eq. (2.50) can be derived:

$$a_{x}^{X}k_{x} + a_{y}^{X}k_{y} = -\frac{1}{4} \left[-a_{x}^{X} \left(k_{x} + \sqrt{3}k_{y} \right) + a_{y}^{X} \left(\sqrt{3}k_{x} - k_{y} \right) \right] + \frac{\sqrt{3}}{4} \eta \left[-a_{x}^{Y} \left(k_{x} + \sqrt{3}k_{y} \right) + a_{y}^{Y} \left(\sqrt{3}k_{x} - k_{y} \right) \right].$$

$$(2.65)$$

And similarly for the \hat{Y} component

$$a_{x}^{Y}k_{x} + a_{y}^{Y}k_{y} = -\frac{1}{4} \left[-a_{x}^{Y} \left(k_{x} + \sqrt{3}k_{y} \right) + a_{y}^{Y} \left(\sqrt{3}k_{x} - k_{y} \right) \right] - \frac{\sqrt{3}}{4} \eta \left[-a_{x}^{X} \left(k_{x} + \sqrt{3}k_{y} \right) + a_{y}^{X} \left(\sqrt{3}k_{x} - k_{y} \right) \right].$$
(2.66)

Since these equations have to hold for all k_x and k_y , separate equations for the k_x and k_y terms can be set up, which gives the following equation in matrix form:

$$\begin{pmatrix} -3 & -\sqrt{3} & -\sqrt{3}\eta & 3\eta \\ \sqrt{3} & -3 & -3\eta & -\sqrt{3}\eta \\ \sqrt{3}\eta & -3\eta & -3 & -\sqrt{3} \\ 3\eta & \sqrt{3}\eta & \sqrt{3} & -3 \end{pmatrix} \begin{pmatrix} a_x^X \\ a_y^X \\ a_x^Y \\ a_y^Y \\ a_y^Y \end{pmatrix} = \mathbf{0}.$$
 (2.67)

The equations in row 2 and row 3 are equivalent as well as the ones in row 1 and row 4. From the equations in the first two rows, it can be found that

$$a_x^X = \eta a_y^Y, \tag{2.68}$$

$$a_y^X = -\eta a_x^Y. (2.69)$$

Together with the finding that the \hat{I} and \hat{Z} component should vanish, the first order Hamiltonian can thus be written as

$$\hat{H}_{\eta}^{(1)} = \eta \left(a_{y}^{Y} k_{x} - a_{x}^{Y} k_{y} \right) \hat{X} + \left(a_{x}^{Y} k_{x} + a_{y}^{Y} k_{y} \right) \hat{Y}. \tag{2.70}$$

For the derivation for this Hamiltonian, however, only the rotational symmetry of the Hamiltonian has been considered. The Hamiltonian already obeys the time reversal symmetry requirement in eq. (2.52), but the mirror symmetry (eq. (2.51)) also requires that $a_x^Y = 0$. Using physical intuition, the first order Hamiltonian can be written as

$$\hat{H}_{\eta}^{(1)} = t_1 a \left(\eta k_x \hat{X} + k_y \hat{Y} \right), \tag{2.71}$$

where a is the lattice constant, the distance between two nearest transition metal or chalcogen atoms, and t_1 represents the effective linear coupling between the conduction band and valence band.

The $\mathbf{k} \cdot \mathbf{p}$ Hamiltonian up to first order is sometimes called the massive Dirac fermion model and was introduced by Xiao et al. in 2012 [16]. It should be noted that the effective linear coupling produces an isotropic band structure around the η K point. In order to understand this, it should be noted that only the magnitude of the coupling will affect the eigenenergies of the two bands, which is given by $t_1 a \sqrt{k_x^2 + k_y^2} = t_1 |\mathbf{k}| a$. Clearly, the magnitude of the coupling only depends on the magnitude of the crystal momentum with respect to the η K point and the band structure is thus isotropic.

The second order To explain the second order terms of the $k \cdot p$ Hamiltonian, it is useful to rewrite the coefficients of the components as

$$a_{2,xx}^{i}k_{x}^{2} + a_{2,yy}^{i}k_{y}^{2} + a_{2,xy}^{i}k_{x}k_{y} = \alpha^{i}(k_{x}^{2} + k_{y}^{2}) + \beta^{i}(k_{x}^{2} - k_{y}^{2}) + 2\gamma^{i}k_{x}k_{y}.$$

$$(2.72)$$

When considering how these terms change under the rotation operation as shown in eq. (2.50), one will get

$$k_x^2 + k_y^2 \to k_x^2 + k_y^2 = |\mathbf{k}|^2,$$
 (2.73)

$$k_x^2 - k_y^2 \to \frac{\sqrt{3}}{2} (2k_x k_y) - \frac{1}{2} (k_x^2 - k_y^2),$$
 (2.74)

$$2k_x k_y \to -\frac{\sqrt{3}}{2} \left(k_x^2 - k_y^2 \right) - \frac{1}{2} \left(2k_x k_y \right). \tag{2.75}$$

As can been seen from these expressions, the $k_x^2 + k_y^2$ term will remain invariant. This means this term, analogous to the zeroth order of the $\mathbf{k} \cdot \mathbf{p}$ Hamiltonian, will only appear in the \hat{I} and \hat{Z} component. The $2k_xk_y$ and $k_x^2 - k_y^2$ terms, on the other hand, transform exactly like k_x and k_y respectively under the rotation operator. These terms will thus appear in the \hat{X} and \hat{Y} in a very similar way as in the first order expression of the $\mathbf{k} \cdot \mathbf{p}$ Hamiltonian. There is a slight difference though: in order to preserve time reversal symmetry given by eq. (2.52), the solution similar to eqs. (2.68) and (2.69) need to be put in a different from:

$$\beta^{Y} = \eta \gamma^{X}, \tag{2.76}$$

$$\gamma^Y = -\eta \beta^X. \tag{2.77}$$

After substituting β^Y and γ^Y in the general expression of the $\mathbf{k} \cdot \mathbf{p}$ Hamiltonian, and considering the mirror symmetry requirement in eq. (2.51), it can be found out that $\gamma^X = 0$. Again using physical intuition, the second order terms of the $\mathbf{k} \cdot \mathbf{p}$ Hamiltonian can be expressed as

$$\hat{H}_{\eta}^{(2)} = \frac{\hbar^2 |\mathbf{k}|^2}{2m_{cb}^{*(1)}} \frac{\hat{I} + \hat{Z}}{2} + \frac{\hbar^2 |\mathbf{k}|^2}{2m_{vb}^{*(1)}} \frac{\hat{I} - \hat{Z}}{2} + t_{3w} a^2 \left[\left(k_x^2 - k_y^2 \right) \hat{X} - 2\eta k_x k_y \hat{Y} \right], \tag{2.78}$$

where $m_{cb}^{*(1)}$ and $m_{vb}^{*(1)}$ are the first order effective masses of the conduction band and valence band respectively, a is the lattice constant, and t_{3w} is an anisotropic coupling term, which will be explained later in more detail.

⁶One may ask whether the rotation in the other direction should be considered. However, this will give the exact same result.

The masses are called the first order effective masses as these terms appear in first order perturbation theory. The second order masses can be obtained by applying second order perturbation theory to the off-diagonal first order $\mathbf{k} \cdot \mathbf{p}$ Hamiltonian, and the actual effective masses can be acquired by using

$$\frac{1}{m_{vb/cb}^*} = \frac{1}{m_{vb/cb}^{*(1)}} + \frac{1}{m_{vb/cb}^{*(2)}}.$$
(2.79)

One of the first derivation of the second order $\mathbf{k} \cdot \mathbf{p}$ Hamiltonian is given by Rostami et al. in 2013 [27]. The second order terms contribute to phenomena in the $\mathbf{k} \cdot \mathbf{p}$ model that cannot be described by the massive Dirac fermion model. The first order effective mass terms are the first terms in the $\mathbf{k} \cdot \mathbf{p}$ model that break the particle-hole symmetry of the system, since usually $m_{cb}^{*(1)} \neq -m_{vb}^{*(1)}$. This is different from the second order effective mass terms, as these terms do not break the particle-hole symmetry because

$$m_{cb}^{*(2)} = -m_{vb}^{*(2)} = \frac{\hbar^2 E_g}{2t_1^2 a^2}. (2.80)$$

Furthermore, the anisotropic coupling term t_{3w} is the first term that break the isotropic behavior of the system around the η K points. This is, however, not directly clear on first sight as the magnitude of the coupling seems isotropic:

$$\sqrt{\left(k_{x}^{2}-k_{y}^{2}\right)^{2}+4k_{x}^{2}k_{y}^{2}} = |\mathbf{k}|^{2}\sqrt{\cos^{4}(\theta)+\sin^{4}(\theta)+2\sin^{2}(\theta)\cos^{2}(\theta)}$$

$$= |\mathbf{k}|^{2}\left(\cos^{2}(\theta)+\sin^{2}(\theta)\right) = |\mathbf{k}|^{2}.$$
(2.81)

However, the phase dependence is different from the linear effective coupling in eq. (2.71) and this will cause triangular shaped contours.

Putting together Putting the terms in eqs. (2.62), (2.71) and (2.78) together and setting $\mu = 0$, the final expression for the $\mathbf{k} \cdot \mathbf{p}$ Hamiltonian is given by

$$\hat{H}_{\eta} = \frac{E_g}{2} (\hat{I} + \hat{Z}) + t_1 a (\eta k_x \hat{X} + k_y \hat{Y}) + \frac{\hbar^2 |\mathbf{k}|^2}{2m_{cb}^{*(1)}} \frac{\hat{I} + \hat{Z}}{2} + \frac{\hbar^2 |\mathbf{k}|^2}{2m_{vb}^{*(1)}} \frac{\hat{I} - \hat{Z}}{2} + t_{3w} a^2 [(k_x^2 - k_y^2) \hat{X} - 2\eta k_x k_y \hat{Y}].$$
(2.82)

This second order $\mathbf{k} \cdot \mathbf{p}$ model is the same as the one given in Fang et al.'s paper on the 11-band model (eq. 10) [25], but different parameter names are used. In table 2.3, the conversion from Fang et al.'s parameters to the parameters in this thesis are shown as well the values for MoS₂, MoSe₂, WS₂, and WSe₂. Plots of the band structure near the η K point (without SOI) of MoS₂ and WSe₂ are given in fig. 2.5. For these plots, the first principle fit parameters from table VI in Fang et al. are used.

Table 2.3: Conversion from Fang et al.'s $\mathbf{k} \cdot \mathbf{p}$ parameters to parameters described in this text as well as the converted values for MoS₂ and WSe₂. The energies and couplings are in eV while the effective masses are in \hbar^2 Å⁻² eV⁻¹.

| | | | material | | |
|-----------------|---|---------|----------|---------|---------|
| param. | expression | MoS_2 | $MoSe_2$ | WS_2 | WSe_2 |
| E_g | f_0 | 1.6735 | 1.4415 | 1.8126 | 1.5455 |
| t_1 | f_1 | 1.1518 | 0.9560 | 1.4073 | 1.1894 |
| $m_{cb}^{*(1)}$ | $\hbar^{2} \left[2a^{2} (f_{2} + f_{3}) \right]^{-1}$ $\hbar^{2} \left[2a^{2} (f_{2} - f_{3}) \right]^{-1}$ | 3.7744 | 453.6217 | 0.3593 | 0.4050 |
| $m_{vb}^{*(1)}$ | $\hbar^2 \Big[2a^2(f_2 - f_3) \Big]^{-1}$ | 0.3644 | 0.4596 | 0.2865 | 0.3635 |
| t_{3w} | f_4 | -0.0780 | -0.0654 | -0.0709 | -0.0627 |
| λ_{vb} | f_5 | 0.0746 | 0.0929 | 0.2153 | 0.2335 |
| λ_{cb} | f_6 | -0.0015 | -0.0106 | 0.0148 | 0.0180 |
| m_{cb}^* | see eq. (2.85) | 0.0614 | 0.0715 | 0.0402 | 0.0442 |
| m_{vb}^* | see eq. (2.86) | -0.0753 | -0.0847 | -0.0537 | -0.0574 |

For small k_x , k_y , the first and second order terms of the $\mathbf{k} \cdot \mathbf{p}$ Hamiltonian can be treated as a perturbation with respect to the zeroth order. Second order perturbation theory can be used to derive an approximate expression for the energy levels of the conduction band and valence band. Anisotropic coupling will be neglected first, i.e. $t_{3w} = 0$. In that case, the energy levels are quite easy to derive:

$$E_{cb} \approx E_g + \frac{\hbar^2 |\mathbf{k}|^2}{2m_{cb}^{*(1)}} + \frac{t_1^2}{E_g} |\mathbf{k}|^2 a^2,$$
 (2.83)

$$E_{vb} \approx \frac{\hbar^2 |\mathbf{k}|^2}{2m_{vb}^{*(1)}} - \frac{t_1^2}{E_g} |\mathbf{k}|^2 a^2.$$
 (2.84)

From these expressions it is also easy to derive the actual effective masses of the conduction band and valence band:

$$\frac{1}{m_{cb}^*} = \frac{1}{\hbar^2} \left. \frac{\partial^2 E_{cb}}{\partial |\mathbf{k}|^2} \right|_{\mathbf{k}=\mathbf{0}} = \frac{1}{m_{cb}^{*(1)}} + \frac{2t_1^2 a^2}{\hbar^2 E_g},\tag{2.85}$$

$$\frac{1}{m_{vb}^*} = \frac{1}{\hbar^2} \left. \frac{\partial^2 E_{vb}}{\partial |\mathbf{k}|^2} \right|_{\mathbf{k}=\mathbf{0}} = \frac{1}{m_{vb}^{*(1)}} - \frac{2t_1^2 a^2}{\hbar^2 E_g}.$$
 (2.86)

Note that these expressions are consistent with eqs. (2.79) and (2.80). The numeric values of the effective masses for MoS₂, MoSe₂, WS₂, and WSe₂ are given in table 2.3.

Now, consider the effect of anisotropic coupling, i.e. $t_{3w} \neq 0$. In that case, the second order correction to the energy for the conduction band (+) and valence band (–) is given by

$$E_{cb/vb}^{(2)} = \pm \frac{t_1^2 |\mathbf{k}|^2 a^2 + t_{3w}^2 |\mathbf{k}|^4 a^4 + 2\eta t_1 t_{3w} |\mathbf{k}|^3 a^3 \cos(3\theta)}{E_{\sigma}},$$
(2.87)

where θ represents the angle of the **k** vector with respect to the *x*-axis. It can be thus seen in this expression that the anisotropic coupling causes triangular anisotropic energy contours, but as suggested earlier about eq. (2.81), this will only be visible if there is an effective linear coupling t_1 .

2.3.2 Spin-orbit interaction

As discussed in the 11-band model, the z component of the spin is (approximately) a good quantum number due to the \hat{M}_{xy} symmetry. Furthermore, the splitting at the $-\eta K$ points is reversed with the respect to the splitting at the ηK points. The spin-orbit interaction can therefore be described with the following Hamiltonian:

$$\hat{H}_{SOI} = \eta \lambda_{cb} \frac{\hat{I} + \hat{Z}}{2} \hat{S}_z + \eta \lambda_{vb} \frac{\hat{I} - \hat{Z}}{2} \hat{S}_z, \tag{2.88}$$

where S_z is the Pauli-Z matrix acting in the spin space, and λ_{cb} and λ_{vb} represent the strength of the spin-orbit interaction of the conduction band and valence band respectively. This is related to the energy splitting at the η K point according to

$$\lambda_{cb/vb} = \eta \frac{E_{cb/vb,\uparrow} - E_{cb/vb,\downarrow}}{2}.$$
 (2.89)

Note that λ_{cb} can be negative since it is possible that $E_{cb,\uparrow} < E_{cb,\downarrow}$. The source of this are the *p*-orbitals at the chalcogen atoms, as already demonstrated in the 11-band tight binding model discussed in section 2.2.

Using the fit parameters in Fang et al., The band structures near the +K point of MoS_2 and WSe_2 are visualized in fig. 2.6. It can clearly be seen from these figures that MoS_2 has a crossing of the spin-up and spin-down conduction band, whereas WSe_2 does not have such a crossing. In order to explain this difference between MoS_2 and WSe_2 , Two things need to be shown: (1) the condition when the spin-up band is lower in energy than the spin-down band at the +K point, and (2) the fact that the spin-up band seemingly has a lower effective mass than the spin-down band at the +K point. The first condition is already explained earlier and this is satisfied when $\lambda_{cb} < 0$. The second condition is more tricky and requires to apply third order perturbation theory. To keep the expression simple, the anisotropic coupling term will be ignored. Treating the spin-orbit interaction

⁷Small k_x , k_y implies that the first and second order terms of the $\mathbf{k} \cdot \mathbf{p}$ Hamiltonian are much smaller than the bandgap.

⁸Anisotropic coupling does not affect the effective mass at the +K point anyway.

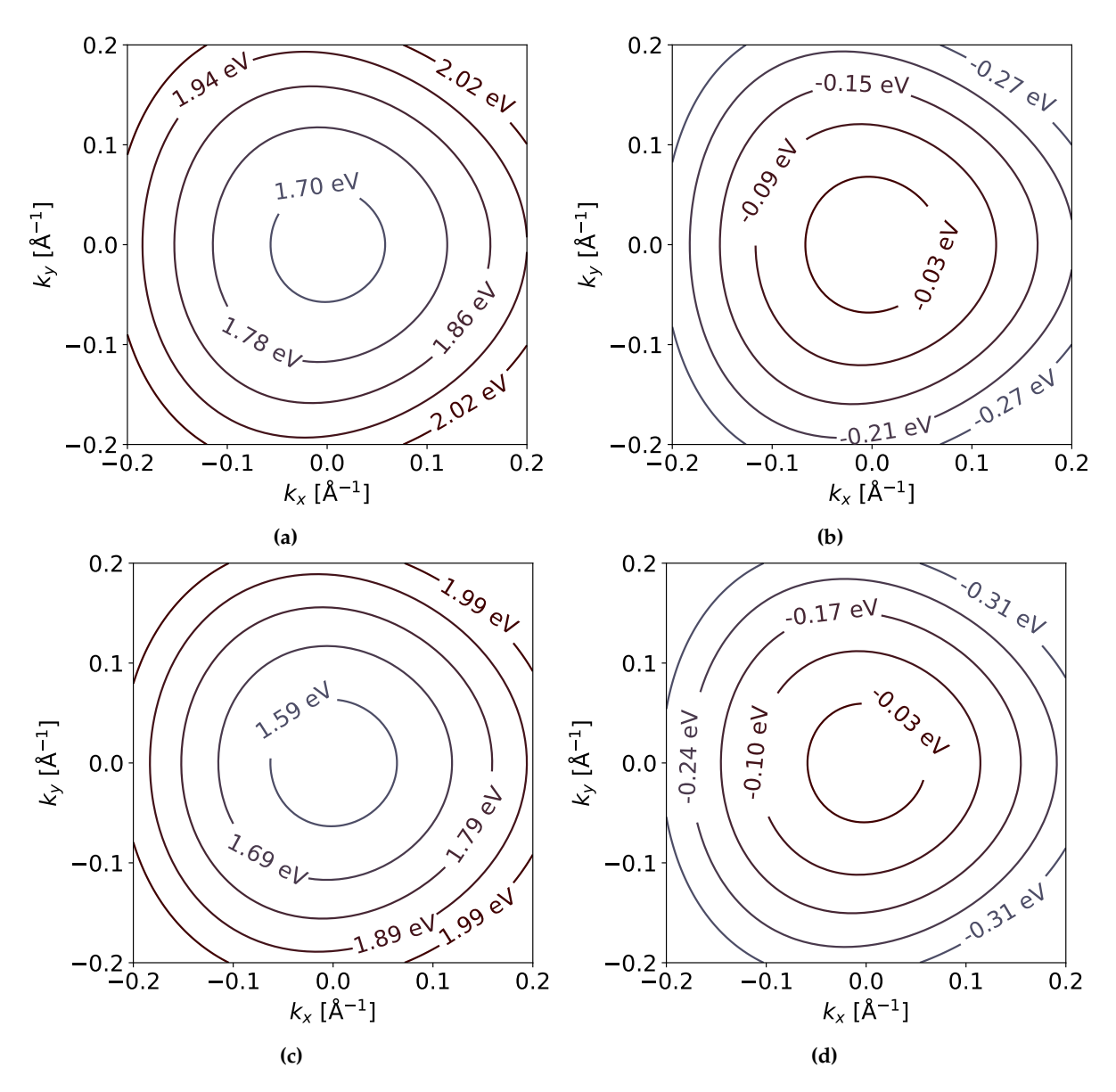


Figure 2.5: Contour plots of: (a) the conduction band of MoS_2 ; (b) the valence band of MoS_2 ; (c) the conduction band of WSe_2 ; (d) the valence band of WSe_2 . These plots are exact solutions of the Hamiltonian near the +K point given in eq. (2.82). Note that SOI has not been included. The anisotropic coupling effect is particularly visible in the valence band.

given in eq. (2.88) as an additional perturbation, an approximate expression can be derived for the eigenenergy of the conduction bands using third order perturbation theory and is given by

$$E_{cb,s} \approx E_g + \eta \lambda_{cb} s + \frac{\hbar^2 |\mathbf{k}|^2}{2m_{cb}^{*(1)}} + \frac{t_1^2 |\mathbf{k}|^2 a^2}{E_g} \left[1 + \frac{\hbar^2 |\mathbf{k}|^2 \left(1/2m_{vb}^{*(1)} - 1/2m_{cb}^{*(1)} \right) + \eta (\lambda_{vb} - \lambda_{cb}) s}{E_g} \right], \tag{2.90}$$

where s is either +1 or -1 representing the spin-up band and spin-down band respectively. The effective mass at the +K point ($\eta = 1$) of these bands is thus given by

$$\frac{1}{m_{cb,s}^*} = \frac{1}{\hbar^2} \left. \frac{\partial^2 E_{cb,s}}{\partial |\mathbf{k}|^2} \right|_{\mathbf{k}=\mathbf{0},\eta=1} = \frac{1}{m_{cb}^{*(1)}} + \frac{2t_1^2 a^2}{\hbar^2 E_g} \left(1 + \frac{\lambda_{vb} - \lambda_{cb}}{E_g} s \right). \tag{2.91}$$

As discussed in the earlier sections, the spin splitting of the conduction band is smaller than that at the valence band, i.e. $|\lambda_{cb}| < |\lambda_{vb}|$. Furthermore, the energy splittings of spin-up and spin-down are much smaller than the bandgap energy, i.e. $|\lambda_{cb}|, |\lambda_{vb}| \ll E_g$. Using this information, it is clear from eq. (2.91) that the effective mass of the spin-up (s=+1) band is lower than that of the spin-down band (s=-1), regardless whether λ_{cb} is positive or negative. It can thus be concluded that crossing of spin-up and spin-down in the conduction band will occur if $\lambda_{cb} < 0$.

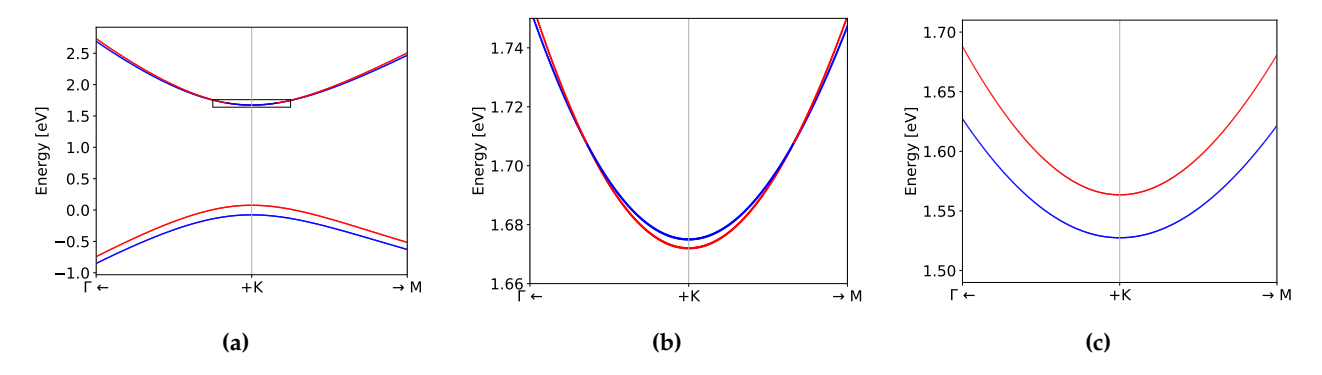


Figure 2.6: (a) The band structure near the +K point of MoS_2 . Red indicates spin-up bands while blue indicates spin-down bands; (b) zoom at the minimum of the conduction band of MoS_2 indicated with rectangle in (a); (c) The minimum of the conduction band near the +K point of WS_2 . Unlike MoS_2 , there is no vanishing SOI.

It is useful later on to have an effective Hamiltonian of the spin-up and spin-down conduction band when superconductivity will be included in the system. This can be done by calculating the third order energy of the spin-up band and spin-down band separately and use them as diagonal elements of the effective Hamiltonian. As mentioned several times earlier, the z-component of the spin is a good quantum number and thus there should be no coupling between these two bands. Furthermore, it is assumed that $|\mathbf{k}|$ is so small that all terms of order $|\mathbf{k}|^4$ or higher can be neglected and this results in an effective Hamiltonian given by

$$\hat{H}_{eff,\eta} = E_g + \frac{\hbar^2 |\mathbf{k}|^2}{2m_{cb}^{*(1)}} + \eta \lambda_{cb} \hat{S}_z + \frac{t_1^2 |\mathbf{k}|^2 a^2 + 2\eta t_1 t_{3w} |\mathbf{k}|^3 a^3 \cos(3\theta)}{E_g} \left[1 + \eta \frac{\lambda_{vb} - \lambda_{cb}}{E_g} \hat{S}_z \right]. \tag{2.92}$$

In literature about Ising superconductivity such as Wang et al.[19], the spin-independent anisotropic term $2\eta t_1 t_{3w} |\mathbf{k}|^3 a^3 \cos(3\theta)/E_g$ is left out as this term does not significantly change the band structure when comparing with the valence band. This also simplifies analytical analysis, which will be done in more detail in section 3.2.2.

Chapter 3

Ising superconductivity

In this chapter, the concept of Ising superconductivity will be explained. The main difference of Ising superconductivity with respect to conventional superconductivity is that Ising SOI needs to be included (hence the name). In this thesis, a general model for (s-wave) superconductivity will be provided in section 3.1 using Bogoliubov-De Gennes (BdG) formalism. In the next section (section 3.2.2), the model will also be applied to the $\mathbf{k} \cdot \mathbf{p}$ model of the TMD monolayer explained in section 2.3. Although the $\mathbf{k} \cdot \mathbf{p}$ model makes it much simpler to analytically analyze the TMD monolayer to a limited extent, it is more convenient to use numerical models, which will be done in the next chapter. In the second-last section (section 3.3), more details will be given about the topological phase in Ising superconductors. This will not be an extensive discussion about topology, but rather the conditions for topology will be specified. In the last section, the findings obtained from the BdG formalism will be compared to scientific literature.

3.1 Basic theory on superconductivity

The source of superconductivity in many-body systems is a small attractive interaction between electrons due to electron-phonon interaction [28]. Such a weak attraction causes electron pairing near the Fermi surface and these electron pairs have a lower energy than two separated electrons near the Fermi surface. An attractive interaction thus causes the Fermi sphere to break down as it is higher in energy than paired electrons. According to the BCS theory [29], the pairing should be between electrons with opposite crystal momentum and spin in order to minimize the energy. These pairs also known as Cooper pairs. Furthermore, it is assumed that the attractive interaction is isotropic and thus independent of the crystal momentum of the electrons. However, it should also be noted that the attractive interaction is only between electrons that are close to the Fermi level due to the fact that phonons can carry only a limited amount of energy called the Debye energy. Cooper pairs and isotropic interaction are the foundation of conventional *s*-wave superconductivity this will also be applied to Ising superconductors.

3.1.1 Hamiltonian

The Hamiltonian of a superconductor consist of two parts: the normal phase Hamiltonian and the Hamiltonian for the attractive interaction. Using the two postulates of *s*-wave superconductivity mentioned in the beginning of this section, the Hamiltonian can be expressed like

$$\hat{H} = \sum_{\mathbf{k}} \sum_{\sigma',n';\sigma,n} \left(\langle \sigma', n' | \hat{H}_{N}(\mathbf{k}) | \sigma, n \rangle - \mu \delta_{\sigma',\sigma} \delta_{n',n} \right) \hat{c}_{\mathbf{k}\sigma'n'}^{\dagger} \hat{c}_{\mathbf{k}\sigma n} - V \sum_{\mathbf{k},\mathbf{l},n',n} \hat{c}_{\mathbf{k}\uparrow n'}^{\dagger} \hat{c}_{-\mathbf{k}\downarrow n'} \hat{c}_{-\mathbf{l}\downarrow n} \hat{c}_{\mathbf{l}\uparrow n}
= \hat{H}_{0} + \hat{H}_{int},$$
(3.1)

where μ is the chemical potential, V is the isotropic attractive interaction, and $\hat{c}^{\dagger}_{\mathbf{k}\sigma n}$ ($\hat{c}_{\mathbf{k}\sigma n}$) is the creation (annihilation) operator for an electron with crystal momentum \mathbf{k} , spin σ and orbital n. Note that the summation is only over states that lie close enough to the chemical potential, due to the fact that phonons only have a maximum amount of energy to couple Cooper pairs. The second term of the Hamiltonian represents the interaction between two different Cooper pairs. Due to the fact that this term has 4 creation/annihilation operators, it is not possible to exactly solve the Schrödinger equation, i.e. finding the eigenvalues and eigenvectors of the Hamiltonian. However, a mean field approximation can be performed, so that this term only has 2 creation/annihilation operators left, which makes diagonalization of the Hamiltonian possible. To this end,

define

$$b_{\mathbf{k}} = \left\langle \sum_{n} \hat{c}_{-\mathbf{k}\downarrow n} \hat{c}_{\mathbf{k}\uparrow n} \right\rangle. \tag{3.2}$$

The trick is then to add and subtract $b_{\mathbf{k}}$ from the $\sum_{n} \hat{c}_{-\mathbf{k}\downarrow n} \hat{c}_{\mathbf{k}\uparrow n}$ terms in the interaction Hamiltonian. The idea is that $\sum_{n} \hat{c}_{-\mathbf{k}\downarrow n} \hat{c}_{\mathbf{k}\uparrow n}$ only slightly deviates from it's mean given by $b_{\mathbf{k}}$, so that $\left(\sum_{n} \hat{c}_{-\mathbf{k}\downarrow n} \hat{c}_{\mathbf{k}\uparrow n} - b_{\mathbf{k}}\right)^{2}$ is negligible. The interaction term of the Hamiltonian after mean field approximation is thus

$$\hat{H}_{int} = -V \sum_{\mathbf{k},\mathbf{l}} \left(b_{\mathbf{k}}^* \left[\sum_{n} \hat{c}_{-\mathbf{k}\downarrow n} \hat{c}_{\mathbf{k}\uparrow n} \right] + b_{\mathbf{l}} \left[\sum_{n} \hat{c}_{\mathbf{l}\uparrow n}^{\dagger} \hat{c}_{-\mathbf{l}\downarrow n}^{\dagger} \right] - b_{\mathbf{k}}^* b_{\mathbf{l}} \right). \tag{3.3}$$

Next step is to define the superconducting pairing as

$$\Delta = V \sum_{\mathbf{l}} b_{\mathbf{l}},\tag{3.4}$$

so that the interaction Hamiltonian can be simplified further to

$$\hat{H}_{int} = -\sum_{\mathbf{k},n} \left(\Delta^* \hat{c}_{-\mathbf{k}\downarrow n} \hat{c}_{\mathbf{k}\uparrow n} + \Delta \hat{c}_{\mathbf{k}\uparrow n}^{\dagger} \hat{c}_{-\mathbf{k}\downarrow n}^{\dagger} - \Delta b_{\mathbf{k}}^* \right). \tag{3.5}$$

Using the commutation relations for electron creation/annihilation operators, the normal phase and interaction Hamiltonian can be rewritten as

$$\hat{H}_{0} = \frac{1}{2} \sum_{\mathbf{k}} \sum_{\sigma', n': \sigma, n} \left(\langle \sigma', n' | \hat{H}_{N}(\mathbf{k}) | \sigma, n \rangle - \mu \delta_{\sigma', \sigma} \delta_{n', n} \right) \left(\hat{c}_{\mathbf{k}\sigma'n'}^{\dagger} \hat{c}_{\mathbf{k}\sigma n} - \hat{c}_{\mathbf{k}\sigma n} \hat{c}_{\mathbf{k}\sigma'n'}^{\dagger} + \delta_{\sigma', \sigma} \delta_{n', n} \right)$$
(3.6)

$$\hat{H}_{int} = \frac{1}{2} \sum_{\mathbf{k},n} \left[\Delta^* \left(\hat{c}_{\mathbf{k}\uparrow n} \hat{c}_{-\mathbf{k}\downarrow n} - \hat{c}_{-\mathbf{k}\downarrow n} \hat{c}_{\mathbf{k}\uparrow n} \right) + \Delta \left(\hat{c}_{-\mathbf{k}\downarrow n}^{\dagger} \hat{c}_{\mathbf{k}\uparrow n}^{\dagger} - \hat{c}_{\mathbf{k}\uparrow n}^{\dagger} \hat{c}_{-\mathbf{k}\downarrow n}^{\dagger} \right) + 2\Delta b_{\mathbf{k}}^* \right], \tag{3.7}$$

and that the total Hamiltonian can be rewritten as

$$\hat{H} = \frac{1}{2} \sum_{\mathbf{k}} \hat{C}_{\mathbf{k}}^{\dagger} \hat{H}_{BdG} \hat{C}_{\mathbf{k}} + \frac{\text{Tr} \left[\hat{H}_N - \mu \hat{I} \right]}{2} + \frac{|\Delta|^2}{V}, \tag{3.8}$$

where

$$\hat{C}_{\mathbf{k}} = \left[\hat{c}_{\mathbf{k}\uparrow 1}, \dots, \hat{c}_{\mathbf{k}\uparrow n}, \hat{c}_{\mathbf{k}\downarrow 1}, \dots, \hat{c}_{\mathbf{k}\downarrow n}, \hat{c}_{-\mathbf{k}\uparrow 1}^{\dagger}, \dots, \hat{c}_{-\mathbf{k}\uparrow n}^{\dagger}, \hat{c}_{-\mathbf{k}\downarrow 1}^{\dagger}, \dots, \hat{c}_{-\mathbf{k}\downarrow n}^{\dagger}\right]^{T}, \tag{3.9}$$

and

$$\hat{H}_{BdG}(\mathbf{k}) = \begin{bmatrix} \hat{H}_N(\mathbf{k}) - \mu \hat{\sigma}_0 \otimes \hat{I}_n & -i\Delta \hat{\sigma}_y \otimes \hat{I}_n \\ i\Delta^* \hat{\sigma}_y \otimes \hat{I}_n & -\hat{H}_N^*(-\mathbf{k}) + \mu \hat{\sigma}_0 \otimes \hat{I}_n \end{bmatrix}, \tag{3.10}$$

which is also known as the Bogoliubov-de Gennes (BdG) Hamiltonian. Further, $\hat{\sigma}_0$ and $\hat{\sigma}_y$ are the identity matrix and Pauli-y matrix in spin space respectively, and I_n is the identity matrix acting in the orbital space.

The next step is to diagonalize the BdG Hamiltonian. By calculating the eigenvalues and eigenvectors of the BdG Hamiltonian, the BdG Hamiltonian can be rewritten as

$$\hat{H}_{BdG}(\mathbf{k}) = \hat{U}_{\mathbf{k}} \hat{D}_{BdG}(\mathbf{k}) \hat{U}_{\mathbf{k}'}^{\dagger} \tag{3.11}$$

where \hat{U} is a matrix with all normalized eigenvectors in the columns and \hat{D}_{BdG} is a diagonal matrix with all the corresponding eigenvalues. The total Hamiltonian can then be rewritten as

$$\hat{H} = \frac{1}{2} \sum_{\mathbf{k}} \hat{P}_{\mathbf{k}}^{\dagger} \hat{D}_{BdG}(\mathbf{k}) \hat{P}_{\mathbf{k}} + \frac{\text{Tr} \left[\hat{H}_N - \mu \hat{I} \right]}{2} + \frac{|\Delta|^2}{V} = \frac{1}{2} \sum_{\mathbf{k},i} \varepsilon_{\mathbf{k},i} \hat{P}_{\mathbf{k},i}^{\dagger} \hat{P}_{\mathbf{k},i} + \frac{\text{Tr} \left[\hat{H}_N - \mu \hat{I} \right]}{2} + \frac{|\Delta|^2}{V}, \tag{3.12}$$

where $\hat{P}_{\mathbf{k}} = \hat{U}_{\mathbf{k}}^{\dagger} \hat{C}_{\mathbf{k}'}$ and $\hat{p}_{\mathbf{k},i}^{\dagger}$ ($\hat{p}_{\mathbf{k},i}$) is the new creation (annihilation) operator for quasi-particles and quasi-holes in the superconductor, which are sometimes called Bogoliubons. As the basis of the original BdG Hamiltonian in eq. (3.10) contains both particles and holes, so does the diagonalized Hamiltonian. In order to find the ground state and the exited states of the Hamiltonian, this has to be kept in mind: if a quasi-particle in stat i

 $^{^{1}}$ The superconducting pairing may be a complex value, but since only a single bulk TMD monolayer will be studied, the phase will not be interesting.

is present, then there is no quasi-hole in state i. However, if a creation operator for a quasi-particle is known, then the creation operator for the corresponding hole can be found using the particle-hole symmetry of the BdG Hamiltonian, which says

$$\hat{\mathcal{P}}\hat{H}_{BdG}(\mathbf{k})\hat{\mathcal{P}} = -\hat{H}_{BdG}(-\mathbf{k}),\tag{3.13}$$

where, in this case, $\hat{\mathcal{P}} = \tau_x \hat{\mathcal{K}}$, with τ_x the Pauli-x matrix in particle-hole space and $\hat{\mathcal{K}}$ the complex conjugation operator. So if the creation operators create a quasi-particle with energy $\varepsilon_{\mathbf{k},i} > 0$, then there are creation operators $\hat{\mathcal{P}}\hat{P}^{\dagger}_{-\mathbf{k}}$ that create the corresponding quasi-hole with energy $-\varepsilon_{\mathbf{k},i}$. Therefore, in order to find the ground state, all the quasi-hole creation operators should be converted in to quasi-particle creation operators using the fermion commutation relation $\{\hat{p},\hat{q}\}=1$. The total Hamiltonian with only the quasi-particle creation operators is thus

$$\hat{H} = \sum_{\varepsilon_{\mathbf{k},i}>0} \varepsilon_{\mathbf{k},i} \left(\hat{p}_{\mathbf{k},i}^{\dagger} \hat{p}_{\mathbf{k},i} - \frac{1}{2} \right) + \frac{\text{Tr} \left[\hat{H}_N - \mu \hat{I} \right]}{2} + \frac{|\Delta|^2}{V}. \tag{3.14}$$

From this expression, it can be found that the ground state energy of the superconductor is given by²

$$E_g = \frac{\text{Tr}\left[\hat{H}_N\right]}{2} + \frac{|\Delta|^2}{V} - \frac{1}{2} \sum_{\varepsilon_{\mathbf{k},i} > 0} \varepsilon_{\mathbf{k},i}.$$
(3.15)

Furthermore, the excitation energies of the superconductor are $\varepsilon_{\mathbf{k},i} > |\Delta|$. Unlike in normal conductors, where excitation energies are infinitely small, superconductors will have hardly any scattering (and therefore zero resistance) as a minimum energy of $|\Delta|$ is required to perturb the ground state of the superconductor.

3.1.2 Obtaining the weak-coupling limit

In order to find the superconducting pairing Δ , the free energy needs to be minimized. The obtained superconducting pairing should also be consistent with the self-consistent gap equation (eq. (3.4)). This equation, however, may give non-trivial solutions ($\Delta \neq 0$), which do not globally minimize the free energy. On the other hand, the self-consistent gap equation can be used when the isotropic interaction V needs to be calculated, if Δ_0 , the superconducting pairing at zero temperature and field, is known. Using the definitions specified earlier in section 3.1.1, the expression of b_k can be rewritten as

$$b_{\mathbf{k}} = -\left\langle \sum_{n} \hat{c}_{\mathbf{k} \uparrow n} \hat{c}_{-\mathbf{k} \downarrow n} \right\rangle = -\left\langle \operatorname{Tr}_{\text{topright}} \left[\hat{C}_{\mathbf{k}} \hat{C}_{\mathbf{k}}^{\dagger} \right] \right\rangle = -\operatorname{Tr}_{\text{topright}} \left[\hat{U}_{\mathbf{k}} \left\langle \hat{P}_{\mathbf{k}} \hat{P}_{\mathbf{k}}^{\dagger} \right\rangle \hat{U}_{\mathbf{k}}^{\dagger} \right], \tag{3.16}$$

where ${\rm Tr}_{\rm topright}$ indicates that the trace should be applied to the top right $n\times n$ submatrix of $\hat{C}_{\bf k}\hat{C}_{\bf k}^{\dagger}$, which is a $4n\times 4n$ matrix. To evaluate $\langle\hat{P}_{\bf k}\hat{P}_{\bf k}^{\dagger}\rangle$, note that the diagonal matrix elements are simply unity minus the average occupation of the quasi-particles or quasi-holes, which can be calculated using the Fermi-Dirac distribution. On the other hand, the off-diagonal elements should be zero as eigenstates of the BdG Hamiltonian do not contribute to the average of a creation-annihilation pair of two different states. The matrix elements of $\langle\hat{P}_{\bf k}\hat{P}_{\bf k}^{\dagger}\rangle$ are thus given by

$$\langle \hat{p}_{\mathbf{k},i} \hat{p}_{\mathbf{k},j}^{\dagger} \rangle = \begin{cases}
0 & \text{if } i \neq j \\
1 - \frac{1}{\exp\left(-\frac{c_{\mathbf{k},i}}{k_B T}\right) + 1} & \text{if } i = j
\end{cases}$$

$$= \begin{cases}
0 & \text{if } i \neq j \\
\frac{1}{\exp\left(\frac{c_{\mathbf{k},i}}{k_B T}\right) + 1} & \text{if } i = j
\end{cases}$$
(3.17)

where k_B is the Boltzmann constant and T is the temperature. A problem of using the self-consistent gap equation to calculate V, however, is that it does not look efficient: only the diagonal of a small upper-right part of the matrix is actually used. Fortunately, there is a better way to get V given Δ_0 , but this requires to minimize the free energy as well and the method will be explained later in this section.

From the final Hamiltonian in eq. (3.14), the grand partition function can be derived and is given by

$$Z_{gr} = \exp\left(-\left[\frac{\text{Tr}\left[\hat{H}_N - \mu\hat{I}\right]}{2} + \frac{|\Delta|^2}{V}\right]/k_B T\right) \prod_{\varepsilon_{\mathbf{k},i}>0} 2 \cosh\left(\frac{\varepsilon_{\mathbf{k},i}}{2k_B T}\right). \tag{3.18}$$

 $^{^2}$ The chemical potential μ should not be included when finding the ground state. It is only there for convenience the free energy will be calculated later on.

From this, the free energy³ can then simply be calculated by

$$\Phi = -k_B T \log \left(Z_{gr} \right) = \frac{\text{Tr} \left[\hat{H}_N - \mu \hat{I} \right]}{2} + \frac{|\Delta|^2}{V} - k_B T \sum_{\varepsilon_{\mathbf{k},i} > 0} \log \left(2 \cosh \left(\frac{\varepsilon_{\mathbf{k},i}}{2k_B T} \right) \right). \tag{3.19}$$

For the purpose of finding a Δ that minimizes the free energy the trace term $\text{Tr}\left[\hat{H}_N - \mu\hat{I}\right]/2$ can be left out as it does not depend on Δ . Furthermore, as cosh is an even function, it simpler to sum over all eigenvalues and divide the result by two. This is equivalent as the particle-hole symmetry requires that if there is a quasi-particle with energy ε , then there is a quasi-hole with energy $-\varepsilon$. The expression for the free energy will thus become

$$\Phi = \frac{|\Delta|^2}{V} - \frac{1}{2}k_B T \sum_{\mathbf{k},i} \log\left(2\cosh\left(\frac{\varepsilon_{\mathbf{k},i}}{2k_B T}\right)\right). \tag{3.20}$$

For low temperatures, $\cosh(\varepsilon_{\mathbf{k},i}/2k_BT) \approx \exp(|\varepsilon_{\mathbf{k},i}|/2k_BT)/2$. so that the free energy in that limit becomes

$$\Phi \approx \frac{|\Delta|^2}{V} - \sum_{\mathbf{k},i} \frac{|\varepsilon_{\mathbf{k},i}|}{4}.$$
 (3.21)

This is also the exact value of the free energy if T = 0.

As mentioned earlier, the free energy expression can be used to find V given the superconducting pairing Δ_0 in case of zero temperature and zero field. To this end, the free energy (using the expression for low temperatures eq. (3.21)) needs to be minimized by taking the derivative of eq. (3.20) with respect to $|\Delta|$. This gives the expression

$$\frac{\partial \Phi}{\partial |\Delta|}\Big|_{|\Delta| = |\Delta_0|} = \frac{2|\Delta|}{V} - \frac{1}{4} \sum_{\mathbf{k}, i} \frac{\partial |\varepsilon_{\mathbf{k}, i}|}{\partial |\Delta|}\Big|_{|\Delta| = |\Delta_0|} = 0. \tag{3.22}$$

This still requires to find an expression for $\partial |\varepsilon_{\mathbf{k},i}|/\partial |\Delta| \Big|_{|\Delta|=|\Delta_0|}$. Fortunately, because of the absence of a magnetic field, the normal phase Hamiltonian is time reversal symmetric and this gives a relation between the normal phase eigenstates for opposite \mathbf{k} , as

$$\hat{H}_N(\mathbf{k}) = \hat{\mathcal{T}}^{-1} \hat{H}_N(-\mathbf{k}) \hat{\mathcal{T}}.$$
 (3.23)

The time reversal operator is given by

$$\hat{\mathcal{T}} = \left(i\hat{\sigma}_y \otimes \hat{I}_n\right)\hat{\mathcal{K}}.\tag{3.24}$$

Thus, if there is a quasi-particle in the normal phase with crystal momentum \mathbf{k} , then the time reversal symmetry requires there is a quasi-particle with opposite momentum and spin with the same energy. But these quasi-particles form a Cooper pair together, which means that the BdG Hamiltonian can be block diagonalized such that the blocks look like

$$\hat{H}_{BdG}(\mathbf{k}, n) = \begin{pmatrix} \xi_{\mathbf{k}, n} & \Delta e^{i\varphi} \\ \Delta^* e^{-i\varphi} & -\xi_{\mathbf{k}, n} \end{pmatrix}, \tag{3.25}$$

where $\xi_{\mathbf{k},n}$ represents the the *n*th eigenvalue of the normal phase⁴ at crystal momentum \mathbf{k} , and φ is some phase. The eigenvalues of this block are given by

$$\varepsilon_{\mathbf{k},n} = \pm \sqrt{\xi_{\mathbf{k},n}^2 + |\Delta|^2},\tag{3.26}$$

so that eq. (3.22) can be rewritten as

$$\frac{1}{V} = \frac{1}{4} \sum_{\mathbf{k},n} \frac{1}{\sqrt{\xi_{\mathbf{k},n}^2 + |\Delta_0|^2}}.$$
 (3.27)

From this expression, that it is easier to find V in terms of Δ_0 than with the method explained in the beginning of this section, as only the eigenvalues of the normal phase Hamiltonian are required in addition to Δ_0 . The sum over \mathbf{k} in the expression can also be converted into an integral as the possible crystal momenta form a continuum in large systems and this gives

$$\frac{1}{V} = \frac{1}{4} \sum_{n} \int_{-\hbar\omega_{D}}^{\hbar\omega_{D}} \frac{\mathcal{N}_{n}(\xi) d\xi}{\sqrt{\xi^{2} + |\Delta_{0}|^{2}}},$$
(3.28)

 $^{^3}$ Since the Hamiltonian describes an open system with constant T and μ , it also also known the grand potential, but in the literature, it is usually called the (Landau) free energy.

 $^{^4}$ This eigenvalue is the energy of the nth band with respect to the chemical potential μ .

where $\mathcal{N}_n(\xi)$ represents the density of states (DOS) for the nth band, and ω_D is the Debye frequency. As explained earlier, the attractive interaction between Cooper pairs is due to electron-phonon interaction and the maximum energy of the phonons $\hbar\omega_D$ determines the cutoff energy of the integral. Assuming that the density of states of all the bands are roughly constant in the interval $[-\hbar\omega_D, \hbar\omega_D]$, the integral can also be evaluated so that

$$\frac{1}{\mathcal{N}_{tot}(0)V} = \frac{1}{4} \int_{-\hbar\omega_D}^{\hbar\omega_D} \frac{\mathrm{d}\xi}{\sqrt{\xi^2 + |\Delta_0|^2}} = \frac{1}{2} \sinh^{-1} \left(\frac{\hbar\omega_D}{|\Delta_0|}\right),\tag{3.29}$$

where $\mathcal{N}_{tot}(0) = \sum_n \mathcal{N}_n(0)$ represents the total density of states at the chemical potential. In most superconductors $\mathcal{N}_{tot}(0)V \ll 1$, which is also known as the weak-coupling limit. In that case, it can be found that

$$|\Delta_0| = 2\hbar\omega_D \exp\left(-\frac{2}{N_{tot}(0)V}\right). \tag{3.30}$$

This equation holds for any (time reversal symmetric) system with conventional *s*-wave superconductivity. Note that the weak-coupling limit can also be achieved by imposing $|\Delta_0| \ll \hbar \omega_D$.

3.1.3 Universal critical temperature

At finite temperatures, the general free energy expression (eq. (3.20)) should be used instead. Minimizing the free energy by taking the derivative with respect to $|\Delta|$ gives

$$\frac{1}{V} = \frac{1}{4} \sum_{n} \int_{-\hbar\omega_D}^{\hbar\omega_D} \tanh\left(\frac{\sqrt{\xi^2 + |\Delta|^2}}{2k_B T}\right) \frac{\mathcal{N}_n(\xi) d\xi}{\sqrt{\xi^2 + |\Delta|^2}}.$$
(3.31)

Using this expression, an universal expression for the critical temperature of all conventional *s*-wave superconductors can be derived. At the critical temperature T_c , the superconducting pairing Δ should become zero. Again assuming that the density of states of all the bands are roughly constant in the interval $[-\hbar\omega_D, \hbar\omega_D]$, one can rewrite the expression as

$$\frac{2}{\mathcal{N}_{tot}(0)V} = \frac{1}{2} \int_{-\hbar\omega_D}^{\hbar\omega_D} \tanh\left(\frac{|\xi|}{2k_B T_c}\right) \frac{\mathrm{d}\xi}{|\xi|} = \ln\left(\frac{2\hbar\omega_D}{\pi k_B T_c}\right) + \gamma, \tag{3.32}$$

where $\gamma = 0.577...$ is the so-called Euler's constant. Working out further gives

$$k_B T_c = \frac{2e^{\gamma}}{\pi} \hbar \omega_D e^{-\frac{2}{N_{tot}(0)V}} \approx \frac{|\Delta_0|}{1.764},$$
(3.33)

where the weak-coupling limit (eq. (3.30)) has been used in the last step. This equation fixes the ratio between the critical temperature and the superconducting pairing in the weak-coupling limit and is valid for any material with conventional s-wave pairing as long as $\mathcal{N}_{tot}(0)V \ll 1$.

One may be concerned whether the Δ that minimizes the free energy given by equation eq. (3.31) converges when the Debye energy diverges. By carefully analyzing the equation, it can be found that this is indeed the case and the analysis is given in appendix A.

3.2 Critical magnetic field

In the previous section, it has been shown that there is an universal relation of the critical temperature: eq. (3.33) applies for any time-reversal symmetric normal phase Hamiltonian in the weak-coupling limit. For the critical magnetic field, however, there is no such universal relation, and it depends on the SOI of the material what the critical field will be. In this section, the critical field of a simple 2D free electron model will be discussed first

3.2.1 2D free electron model

The normal phase Hamiltonian of the 2D free electron model without external field is given by

$$\hat{H}_N = \left(\frac{\hbar^2 k^2}{2m_e} - \mu\right) \hat{\sigma}_0. \tag{3.34}$$

When an external field is applied to the system, the two spin states will be split, which is also known as the Zeeman effect. The Hamiltonian due to this external field is given by

$$\hat{H}_{Zeeman} = \frac{1}{2} \mu_B g_e \hat{\boldsymbol{\sigma}} \cdot \mathbf{H}_{ext} \approx \mu_B \hat{\boldsymbol{\sigma}} \cdot \mathbf{H}_{ext}, \tag{3.35}$$

where $\hat{\sigma} = [\hat{\sigma}_x, \hat{\sigma}_y, \hat{\sigma}_z]^T$, μ_B is the Bohr magneton and $g_e \approx 2$ is the gyromagnetic ratio of the electron spin. Plugging the sum of the normal phase Hamiltonian and the Zeeman Hamiltonian in the BdG Hamiltonian (eq. (3.10)) gives

$$\hat{H}_{BdG} = \begin{bmatrix} \frac{\hbar^2 k^2}{2m_e} - \mu + \mu_B H_z & \mu_B \left(H_x - i H_y \right) & 0 & -\Delta \\ \mu_B \left(H_x + i H_y \right) & \frac{\hbar^2 k^2}{2m_e} - \mu - \mu_B H_z & \Delta & 0 \\ 0 & \Delta^* & -\frac{\hbar^2 k^2}{2m_e} + \mu - \mu_B H_z & \mu_B \left(-H_x - i H_y \right) \\ -\Delta^* & 0 & \mu_B \left(-H_x + i H_y \right) & -\frac{\hbar^2 k^2}{2m_e} + \mu + \mu_B H_z \end{bmatrix}$$
(3.36)

The eigenvalues can be derived analytically and are given by

$$\varepsilon_{\mathbf{k}} = \pm \left| \mu_B H_{ext} \pm \sqrt{\left[\frac{\hbar^2 k^2}{2m_e} - \mu \right]^2 + |\Delta|^2} \right|, \tag{3.37}$$

where $H_{ext} = \sqrt{H_x^2 + H_y^2 + H_z^2}$. Plugging these eigenvalues in the expression of the free energy (eq. (3.20)) results in

$$\Phi = \frac{|\Delta|^2}{V} - k_B T \sum_{\mathbf{k}, s = \pm 1} \log \left(2 \cosh \left(\frac{\mu_B H_{ext} + s \sqrt{\left[\frac{\hbar^2 k^2}{2m_e} - \mu \right]^2 + |\Delta|^2}}{2k_B T} \right) \right). \tag{3.38}$$

Taking the derivative with respect to $|\Delta|$ and equating this to zero gives the following expression

$$\frac{\partial \Phi}{\partial |\Delta|} = \frac{2}{V} - \frac{1}{2} \sum_{\mathbf{k}, s = \pm 1} \tanh \left(\frac{\mu_B H_{ext} + s \sqrt{\left[\frac{\hbar^2 k^2}{2m_e} - \mu\right]^2 + |\Delta|^2}}{2k_B T} \right) \frac{s}{\sqrt{\left[\frac{\hbar^2 k^2}{2m_e} - \mu\right]^2 + |\Delta|^2}} = 0, \tag{3.39}$$

and converting summation into integration gives

$$\frac{1}{V} = \frac{1}{4} \sum_{s=\pm 1} \int_{-\hbar\omega_D}^{\hbar\omega_D} \tanh\left(\frac{\mu_B H_{ext} + s\sqrt{\xi^2 + |\Delta|^2}}{2k_B T}\right) \frac{s\mathcal{N}_s(\xi) d\xi}{\sqrt{\xi^2 + |\Delta|^2}}.$$
 (3.40)

In the weak-coupling limit, eqs. (3.30) and (3.33) can be recovered from this equation.

The critical field H_c at zero temperature with respect to the pairing at zero temperature and field $|\Delta_0|$ depends on the type of system. In case of the 2D free electron model, if T=0, $\Delta=\Delta_0$, eq. (3.40) will reduce to eq. (3.29) as long as $\mu_B H_{ext} < |\Delta_0|$. This suggests that at zero temperature, the free energy has an extrema at $\Delta=\Delta_0$ as long as $\mu_B H_{ext} < |\Delta_0|$. However, this does not always mean that the global minimum of the free energy is at that point: the normal phase $\Delta=0$ may minimize the free energy as well. Therefore, in order to find the critical field at zero temperature, one need to compare the free energy of the superconducting phase with that of the normal phase. At the critical field, the difference in free energy should vanish so that

$$\Phi_N - \Phi_S = \frac{\mathcal{N}_{tot}(0)}{4} \sum_{s=\pm 1} \int_{-\hbar\omega_D}^{\hbar\omega_D} \left(\left| \mu_B H_c + s \sqrt{\xi^2 + |\Delta_0|^2} \right| - \left| \mu_B H_c + s |\xi| \right| \right) d\xi - \frac{|\Delta_0|^2}{V} = 0.$$
 (3.41)

Assuming that $\mu_B H_c < |\Delta_0| < \hbar \omega_D$, working out the integral gives

$$\frac{2|\Delta_0|^2}{N_{tot}(0)V} = \hbar\omega_D \sqrt{(\hbar\omega_D)^2 + |\Delta_0|^2} + |\Delta_0|^2 \log\left(\frac{\hbar\omega_D + \sqrt{(\hbar\omega_D)^2 + |\Delta_0|^2}}{|\Delta_0|}\right) - (\mu_B H_c)^2 - (\hbar\omega_D)^2.$$
(3.42)

In the weak-coupling limit, $2/N_{tot}(0)V$ can be substituted using eq. (3.30). As $|\Delta_0| \ll \hbar\omega_D$ in the weak-coupling limit, the expression can be written as a Taylor series. When $\hbar\omega_D \to \infty$, the Taylor series will reduce to

$$\mu_B H_c = \frac{|\Delta_0|}{\sqrt{2}}.\tag{3.43}$$

Substituting the $|\Delta_0|$ for the expression in eq. (3.33) gives

$$\mu_B H_c \approx 1.247 k_B T_c. \tag{3.44}$$

This expression of the critical field is in agreement with that of Clogston [30], and this is commonly known as the Pauli paramagnetic limit.

3.2.2 Superconducting TMD monolayers

The BdG formalism can also be applied to the $\mathbf{k} \cdot \mathbf{p}$ model of the TMD monolayer in section 2.3. The effective $\mathbf{k} \cdot \mathbf{p}$ Hamiltonian given in eq. (2.92) can be rewritten as

$$\hat{H}_{eff,\eta}(\mathbf{k}) = Ak^2 + \left[\eta B + \eta Ck^2 + \left(k_x^3 - 3k_x k_y^2 \right) D \right] \hat{S}_z = Ak^2 + f(\mathbf{k}, \eta, B, C, D) \hat{S}_z, \tag{3.45}$$

where $k = \sqrt{k_x^2 + k_y^2}$ and A, B, C, and D are the material-dependent parameters that can be determined using eq. (2.92). As stated at the end of section 2.3.2, the spin-independent trigonal warping term can be left out to simplify analysis and this is done here as well.

Deriving the superconducting gap as well as the critical field and temperature can be done in a very similar way as in the 2D free electron model in section 3.2.1. The BdG Hamiltonian of a TMD monolayer is given by

$$\hat{H}_{BdG}(\mathbf{k}) = \begin{bmatrix} \hat{H}_{eff,\eta}(\mathbf{k}) + \hat{H}_{Zeeman} - \mu \hat{\sigma}_0 & -i\Delta \hat{\sigma}_y \\ i\Delta^* \hat{\sigma}_y & -\hat{H}_{eff,-\eta}^*(-\mathbf{k}) - \hat{H}_{Zeeman}^* + \mu \hat{\sigma}_0 \end{bmatrix}. \tag{3.46}$$

The eigenvalues can be calculated analytically if the field has no component perpendicular to the TMD monolayer, i.e. it is a fully in-plane field. In that case the eigenvalues are given by

$$\varepsilon_{\mathbf{k}} = \pm \sqrt{\xi_{\mathbf{k}}^2 + f_{\mathbf{k}}^2 + (\mu_B H_{ext})^2 + |\Delta|^2 \pm 2\sqrt{\xi_{\mathbf{k}}^2 \left[f_{\mathbf{k}}^2 + (\mu_B H_{ext})^2 \right] + |\Delta|^2 (\mu_B H_{ext})^2}},$$
(3.47)

where $\xi_{\mathbf{k}} = Ak^2 - \mu$ and $f_{\mathbf{k}} = f(\mathbf{k}, \eta, B, C, D)$ from eq. (3.45).

Just as for the 2D free electron model, an expression for the free energy can be derived and minimized it by setting the derivative of the free energy with respect to the superconducting gap to zero. When the temperature and external field are set to zero, one can derive that

$$\frac{2}{V} = \frac{1}{2} \sum_{\mathbf{k}, s \in S_{\mathbf{k}}} \frac{1}{\sqrt{(|\xi_{\mathbf{k}}| + s|f_{\mathbf{k}}|)^{2} + |\Delta_{0}|^{2}}} = \frac{1}{2} \int_{-\hbar\omega_{D}}^{\hbar\omega_{D}} \frac{\mathcal{N}_{tot}(\xi) d\xi}{\sqrt{\xi^{2} + |\Delta_{0}|^{2}}},$$
(3.48)

where S_k can be either a set with -1 and +1 as elements or -1 as only element. It depends on the energies in the normal phase which set should be picked as these may not lie too far away from the chemical potential. When converting the sum in eq. (3.48) into an integral, one will recover eq. (3.29). Similarly the expression for the critical temperature will be

$$\frac{2}{V} = \frac{1}{2} \sum_{\mathbf{k}, s \in S_{\mathbf{k}}} \frac{1}{||\xi_{\mathbf{k}}| + s|f_{\mathbf{k}}||} \tanh\left(\frac{||\xi_{\mathbf{k}}| + s|f_{\mathbf{k}}||}{2k_B T_c}\right) = \frac{1}{2} \int_{-\hbar\omega_D}^{\hbar\omega_D} \tanh\left(\frac{|\xi|}{2k_B T_c}\right) \frac{\mathcal{N}_{tot}(\xi) d\xi}{|\xi|}, \tag{3.49}$$

which is the same equation as eq. (3.32) when the sum will be properly converted into an integral.

3.3 Topological phase

The possibility of topological superconductivity in TMD monolayers has recently been described by Wang et al[19]. A non-trivial topological superconducting phase will occur if there are k points (also called nodal points) in the superconductor where the energy gap between particle and hole excitations vanish. In normal superconductors without any external field, this does not occur as it is known that in that case the gap between particle and hole excitations is at least $2|\Delta|$. The gap could be closed by means of an external field, but making the field too large will break superconductivity. In case of the 2D free electron model, closing this gap at zero temperature is not possible as the required field strength exceeds the Pauli limit. Ising superconductors, on the other hand, have an enhanced critical field which increases the likelihood to find topological phases. In terms

of BdG formalism, the nodal points can be found at the k points where the eigenvalues become zero. Using the result of the $k \cdot p$ model, nodal points are found when

$$\xi_{\mathbf{k}}^{2} + f_{\mathbf{k}}^{2} + (\mu_{B}H_{ext})^{2} + |\Delta|^{2} - 2\sqrt{\xi_{\mathbf{k}}^{2} \left[f_{\mathbf{k}}^{2} + (\mu_{B}H_{ext})^{2} \right] + |\Delta|^{2} (\mu_{B}H_{ext})^{2}} = 0.$$
 (3.50)

And solving this equation for ξ_k^2 gives

$$\xi_{\mathbf{k}}^{2} = (\mu_{B} H_{ext})^{2} + f_{\mathbf{k}}^{2} - |\Delta|^{2} \pm 2i|\Delta||f_{\mathbf{k}}|. \tag{3.51}$$

In order to have real solutions, either Δ or $f_{\bf k}$ should be zero. However, $\Delta=0$ implies that there is no superconductivity so in order get topological superconductivity, the spin-orbit splitting term $f_{\bf k}$ should vanish. This means that the nodal points should satisfy the following two equations:

$$\eta B + \eta C k^2 + D k^3 \cos(3\theta) = 0, \tag{3.52}$$

$$Ak^{2} = \mu \pm \sqrt{(\mu_{B}H_{ext})^{2} - |\Delta|^{2}}.$$
(3.53)

These equations are equivalent to equations (4a) and (4b) in Wang et al[19].

With the first equation, a minimum and maximum of k can be calculated at which nodal points can be calculated. The k^3 term makes solving exactly tricky, but using the method described by Wang et al., one can approximate eq. (3.52) as

$$k^{2} = -\frac{B}{C} - \frac{\eta D \cos(3\theta)}{C} k^{3} \approx -\frac{B}{C} - \frac{\eta D \cos(3\theta)}{C} \left(-\frac{B}{C}\right)^{3/2}.$$
 (3.54)

Defining $k_0^2 = -B/C > 0$ and noting that D/C < 0, the minimum and maximum of k^2 are given by

$$k_{min}^2 = k_0^2 \left(1 + \frac{D}{C} k_0 \right), \tag{3.55}$$

$$k_{max}^2 = k_0^2 \left(1 - \frac{D}{C} k_0 \right). {(3.56)}$$

This means that nodal points can be found when

$$Ak_{min}^{2} = \mu_{min} < \mu \pm \sqrt{(\mu_{B}H_{ext})^{2} - |\Delta|^{2}} < Ak_{max}^{2} = \mu_{max}.$$
 (3.57)

In Wang et al., a distinction is made when the equation holds for both + and - or only for one of the two signs. These will be called the twelve and six nodal point topological superconducting phase respectively. The region of the chemical potential where SOI vanishes is given by (μ_{min}, μ_{max}) and will also be called the vanishing region. As mentioned in the introduction, it is expected that the critical field is suppressed in this region.

3.4 Comparison with literature

A paper where BdG formalism is used to calculate the critical field is He et al.[31], although their expression of the free energy (equation (1)) differs from eq. (3.20). It can be shown, however, that these equations are equivalent. By using $\cosh(x) = \left[\exp(x) + \exp(-x)\right]/2$, eq. (3.20) can be rewritten as

$$\Phi = \frac{|\Delta|^2}{V} - \frac{1}{2}k_B T \sum_{\mathbf{k},i} \left[\frac{\varepsilon_{\mathbf{k},i}}{4} + \log\left(1 + \exp\left(\frac{-\varepsilon_{\mathbf{k},i}}{k_B T}\right)\right) \right]. \tag{3.58}$$

However, $\sum_{\mathbf{k},i} \varepsilon_{\mathbf{k},i}/4 = 0$ due to the particle-hole symmetry of the BdG Hamiltonian, and equation (1) of He et al. will be recovered⁵. In He et al.'s expression, nothing is mentioned about a cutoff energy. The origin of the cutoff energy has already been explained at the start of the chapter and should already be considered when expressing the Hamiltonian in eq. (3.1).

The derivation of the BdG Hamiltonian in section 3.1.1 is somewhat similar to the Bogoliubov-Valatin [32, 33] transformation method explained in Tinkham [34]. The main difference, however, is that a 'trial transformation' has been used to diagonalize the Hamiltonian in Tinkham, while the BdG formalism explained in section 3.1.1 actually describes a method to find the canonical transformation that diagonalizes the Hamiltonian. An other difference is that the expressions involving density of states are a factor 1/2 off compared to the expressions

 $^{^{5}}$ All summations in He et al. have 1/V (inverse of volume) prefactor in order to obtain energy per unit volume, but for computational purposes and the fact that no positional dependence is assumed, this factor is not relevant in this thesis.

in this thesis. Examples include the expression of the superconducting gap at zero temperature and field in the weak coupling limit (equation (3.34) in Tinkham, eq. (3.30) in this thesis), and the integral expression for the critical temperature (equation (3.51) in Tinkam, eq. (3.33) in this thesis). The reason of this discrepancy has to do with how density of states is defined: in Tinkham, the density of states only involves the spin-up or spin-down particles⁶, while in this thesis, $\mathcal{N}_{tot}(0)$ is the total density of states including both spin-up and spin-down. The additional factor 1/2 in front of $\mathcal{N}_{tot}(0)$ in this thesis is therefore an appropriate correction to the expression in Tinkham. It is also worth to mention that eq. (3.31) is equivalent to the self-consistency equation (3.50) derived in Tinkham.

⁶The derivation in Tinkham is also assumes that there is no SOI.

Chapter 4

Numerical model

This chapter introduces a numerical model of the TMD monolayer, which is based on the BdG formalism explained in the previous chapter. The main purpose of this model is to find the critical field as function of chemical potential and Δ_0 , and topological phase diagrams as function of temperature and external field can also be found. In section 4.1, a description of the model will be provided. Although the numerical analysis in this research has been done with python, the description of the model will be more general so that it can also be applied to other languages. In section 4.2, the model will analyzed critically. This includes the input values of the model, whether the superconducting pairing converges to a specific value in the weak-coupling limit, the uncertainty of the calculations, and the results of the model in the case of no spin-orbit interaction. In section 4.3, the results (i.e. the critical field and topological phase diagram) of the model will be displayed. There will also be a brief discussion how these results can be related to experiments.

4.1 Description of model

The procedure of calculating the critical field consists of roughly 4 steps:

- 1. obtain the $\mathbf{k} \cdot \mathbf{p}$ parameters for the Hamiltonian of the conduction band given by eq. (3.45);
- 2. generate a grid of **k**-points and filter all energies at those points that lie too far away from the chemical potential;
- 3. set the temperature to zero, and find the superconducting pairing as a function of external field by minimizing the free energy;
- 4. find the critical field by finding the the external field for which the superconducting pairing vanishes.

In the next subsections, these steps will be discussed in more detail. Step 1 and 2 are also applicable when one wants to plot a topological phase diagram. From there on, one needs to obtain Δ by minimizing the free energy as function of temperature and external field. The phase at a specific temperature and external field can then be determined by the question if Δ is zero and if there are nodal points according to eq. (3.57).

4.1.1 $k \cdot p$ parameters

As can be seen in eq. (3.45), the $\mathbf{k} \cdot \mathbf{p}$ Hamiltonian can be described by 4 parameters A, B, C, D that are material dependent. In this research, MoS₂, MoSe₂, and MoTe₂ are investigated and the values of the 4 parameters for these materials are shown in table 4.1. These values are based on the calculated parameters from Wang et al.[19]: the values for MoS₂ and MoSe₂ are derived from the $\mathbf{k} \cdot \mathbf{p}$ model described in Fang et al.[25], while the values for MoTe₂ are based on the $\mathbf{k} \cdot \mathbf{p}$ model described by Kormányos et al.[35] For all three materials, the Löwdin partition method has been used [36]. An other derivation of the $\mathbf{k} \cdot \mathbf{p}$ parameters A, B, C, D has been explained in section 2.3. Using this method, the same values for B, C, D can be found for MoS₂ and MoSe₂. For MoTe₂, the correct values B, C, D are more difficult to obtain due to the extra spin dependence of the $\mathbf{k} \cdot \mathbf{p}$ parameters in Kormányos et al., but the results can be retrieved when taking the average. The values for A, however, may differ as the Löwdin partition method gives a different spin-independent term [36].

From the $\mathbf{k} \cdot \mathbf{p}$ parameters, one can also derive the vanishing region (μ_{min} , μ_{max}), which is important to explain nodal topological superconductivity. These values can be computed using eqs. (3.55) to (3.57) in section 3.3, and are shown in table 4.2. The vanishing region is also calculated by Wang et al.[19] (table 1), but the values slightly differ as Wang et al. used an additional approximation.

Table 4.1: The 4 parameters A, B, C, D of eq. (3.45) for MoS₂, MoSe₂, and MoTe₂. Values are based on Wang et al.[19]

| | A [eV Å ²] | <i>B</i> [eV] | C [eV Å ²] | $D [eV Å^3]$ |
|----------|------------------------|---------------|------------------------|--------------|
| MoS_2 | 8.1063 | -0.0015 | 0.3645 | -0.1570 |
| $MoSe_2$ | 6.3500 | -0.0106 | 0.5018 | -0.2279 |
| $MoTe_2$ | 6.1451 | -0.0180 | 0.6964 | -0.6575 |

Table 4.2: The vanishing region for MoS_2 , $MoSe_2$, and $MoTe_2$. All values are in units of meV and are calculated from eqs. (3.55) to (3.57).

| | MoS ₂ | MoSe ₂ | MoTe ₂ |
|-------------|------------------|-------------------|-------------------|
| μ_{min} | 32.4 | 125.3 | 134.7 |
| μ_{max} | 34.3 | 143.0 | 182.9 |

4.1.2 k-point generation

Initially, a grid of **k**-points can be generated by taking the Cartesian product of equally spaced k_x values, equally spaced k_y values and the two different valleys $\eta = \pm 1$. The values for both k_x and k_y will go from $-k_{max}$ to k_{max} , and k_{max} has to be large enough so that all **k**-points are considered that have energies that lie close enough to the chemical potential. At the same time, k_{max} must not be too large in order to minimize noise and computation time. In order to find a good upper bound, one can equate the (lower) eigenvalue of the Hamiltonian in eq. (3.45) with the maximum energy $E_{max} = \mu + E_D$, which gives

$$E_{max} = Ak_{max}^2 \pm \left(B + Ck_{max}^2\right) \pm Dk_{max}^3. \tag{4.1}$$

where \pm must be replaced with either a + or a - such that it maximizes k_{max} . Solving the equation for k_{max} is tricky due to the cubic trigonal warping term, but a similar trick can be done as in section 3.3 when finding the minimum and maximum k for nodal points. Neglecting the trigonal warping term gives a maximum given by

$$k_{0,max} = \sqrt{\frac{E_{max} - B}{A - C}},\tag{4.2}$$

where -B in the numerator and -C in the denominator can be justified by the fact that B < 0 and C > 0. By using the fixed point method, an upper bound for k_{max} can be found, which is given by

$$k_{max} \approx \sqrt{\frac{E_{max} - B - Dk_{0,max}^3}{A - C}} \le k_{0,max} \sqrt{1 - 2\frac{k_{0,max}}{A - C}} D.$$
 (4.3)

The upper bound can be justified by the fact that D < 0 and $|A| \gg |B|$, |C|, |D|. The latter condition ensures that the next iteration of the fixed point method will shift the value for k_{max} much less than the previous one, hence the factor 2 in the upper bound.

Once the grid has been generated, the k-points need to be filtered such that only energies that are close enough to the chemical potential are considered, that is

$$\mu - \hbar \omega_D < \varepsilon_{\mathbf{k}} < \mu + \hbar \omega_D. \tag{4.4}$$

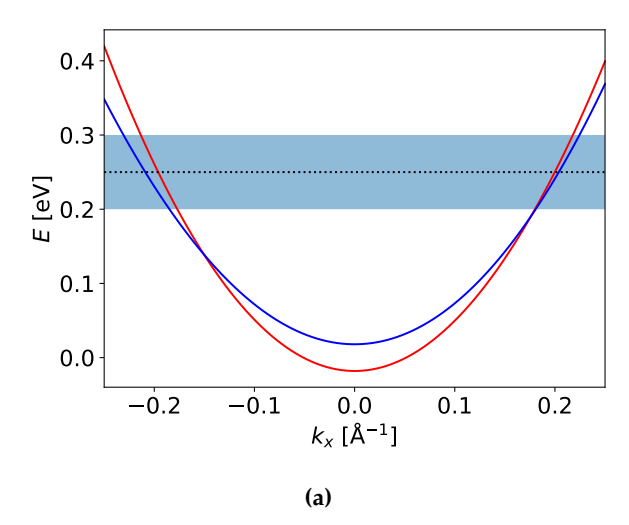
Filling in the expression for the eigenvalues of the BdG Hamiltonian of the TMD monolayer, and setting Δ and the external field to zero, this condition will become

$$||\xi_{\mathbf{k}}| + s|f_{\mathbf{k}}|| < \hbar\omega_D, \tag{4.5}$$

where $\xi_{\mathbf{k}}$ and $f_{\mathbf{k}}$ have the same definition as in eq. (3.47) and $s = \pm 1$. Only the **k** and s that satisfy eq. (4.5) will be considered in the calculation of the free energy.

An example of filtering the **k**-grid for MoTe₂ is demonstrated in fig. 4.1. From fig. 4.1a, it can be seen that the chemical potential μ is set at 0.25 eV and $\hbar\omega_D=0.05$ eV. The selected **k** points in case of $\eta=1$ are indicated in fig. 4.1b¹, which displays an triangularly distorted annulus that lies inside the bounds $[-k_{max}, k_{max}]$ for both k_x and k_y . Note that set of **k**-points that satisfy eq. (4.5) for s=+1 (red region in fig. 4.1b) must be a subset of the **k**-points that satisfy eq. (4.5) for s=-1 (yellow + red region in eq. (4.5)).

¹The case $\eta = -1$ only inverts the distorted annulus shape around the point $\mathbf{k} = \mathbf{0}$



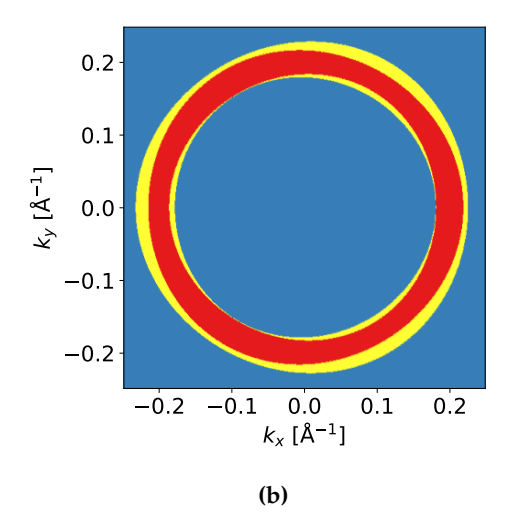


Figure 4.1: Demonstration of filtering of **k**-points. (a) Visualization of the lowest conduction band of MoTe₂ around the K-point obtained from the $\mathbf{k} \cdot \mathbf{p}$ Hamiltonian. The red band is spin-up, the blue band is spin down. The chemical potential (black dotted horizontal line) and the Debye energy (light blue region) are indicated in the figure as well. (b) Grid of **k**-points after filtering, using the chemical potential and Debye energy shown in (a). The blue region are **k**-points that are filtered away, the yellow region are the **k**-points that satisfy eq. (4.5) for s = -1 only, and the red region are the **k**-points that satisfy eq. (4.5) for both s = -1 and s = +1. The upper and lower bound for both k_x and k_y in the figure are k_{max} and $-k_{max}$ respectively, where k_{max} is defined in eq. (4.3).

4.1.3 Minimizing the free energy

Using the **k**-points after filtering, one can now calculate the free energy for any temperature T, external field H_{ext} , and superconducting pairing Δ using the general expression given by eq. (3.20), and the expression for the eigenvalues given by eq. (3.47). The temperature and external field can be chosen freely, but Δ must be such that it minimizes the free energy. In order to find Δ , one needs first to find an expression for the interaction strength V, which can be calculated using eq. (3.27). This expression requires the (maximum) superconducting pairing Δ_0 at zero temperature and field, which will be assumed to be known in this model. Once an expression for V has been found, one can express the free energy as a single variable function $\Phi(\Delta)$ while the temperature and external field will be kept fixed. The Δ that minimizes the free energy should lie between 0 and Δ_0 .

Finding a global minimum of a single variable function in a constrained domain is possible and an algorithm is described by Brent in his book in chapter 6 [37]. This algorithm, however, requires an upper bound of the second derivative of this function. In order to find this upper bound, note that the free energy given by eq. (3.20) consists of two terms: a positive $|\Delta|^2/V$ term and a negative summation term. Using the eigenvalues given by eq. (3.47), it can be derived that the summation term will grow linearly with $|\Delta|$. This implies that the second derivative of the free energy with respect to $|\Delta|$ will converge to 2/V as $|\Delta| \to \infty$. This, however, does not guarantee that the second derivative will stay below 2/V for low $|\Delta|$, so it is required to look at the expression in more detail. At zero temperature and external field, the second derivative of the free energy can be expressed as

$$\frac{\partial^2 \Phi}{\partial |\Delta|^2} = \frac{2}{V} - \sum_{\mathbf{k}, s \in S_{\mathbf{k}}} \frac{(|\xi_{\mathbf{k}}| + s|f_{\mathbf{k}}|)^2}{2(|\Delta|^2 + (|\xi_{\mathbf{k}}| + s|f_{\mathbf{k}}|)^2)^{3/2}} \le \frac{2}{V}.$$
 (4.6)

Thus at zero external field, 2/V is an appropriate upper bound for the second derivative of the free energy. However, this upper bound may not hold in case of finite external fields. This can be seen from the expression of the second derivative of the free energy at $|\Delta| = 0$ (??): the sum term may give positive values for s = -1 if the external field becomes large. If $H_{ext} \to \infty$, the second derivative at T = 0 is then given by

$$\frac{\partial^2 \Phi}{\partial |\Delta|^2} = \frac{2}{V} - \sum_{\mathbf{k}, s \in S_{\mathbf{k}}} \frac{\xi_{\mathbf{k}}^2 s}{2(|\Delta|^2 + \xi_{\mathbf{k}}^2)^{3/2}} \le \frac{2}{V} + \sum_{\mathbf{k} \in S_{-}} \frac{1}{2|\xi_{\mathbf{k}}|},\tag{4.7}$$

where S_{-} denotes the set of **k**-points that satisfies eq. (4.5) only if s = -1. As higher temperatures only weaken the Δ -dependence of the sum term of the free energy, eq. (4.7) is a safe upper bound.

In fig. 4.2, plots of the free energy at zero temperature for several magnetic fields are displayed for MoSe₂. For all figures, $\mu = 0.13 \, \text{eV}$, $\hbar \omega_D = 30 \, \text{meV}$, and $\Delta_0 = 1 \, \text{meV}$. A 500×500 equally spaced **k**-point grid has been used during computation and the sizing and filtering of this grid has been done in agreement with the procedure

described in section 4.1.2. The vertical dotted line indicates the Δ that minimizes the free energy according to Brent's algorithm mentioned earlier. It can be seen that in all cases, the algorithm picks the correct Δ so the issue of a too low upper bound for the second derivative does not arise in this case.

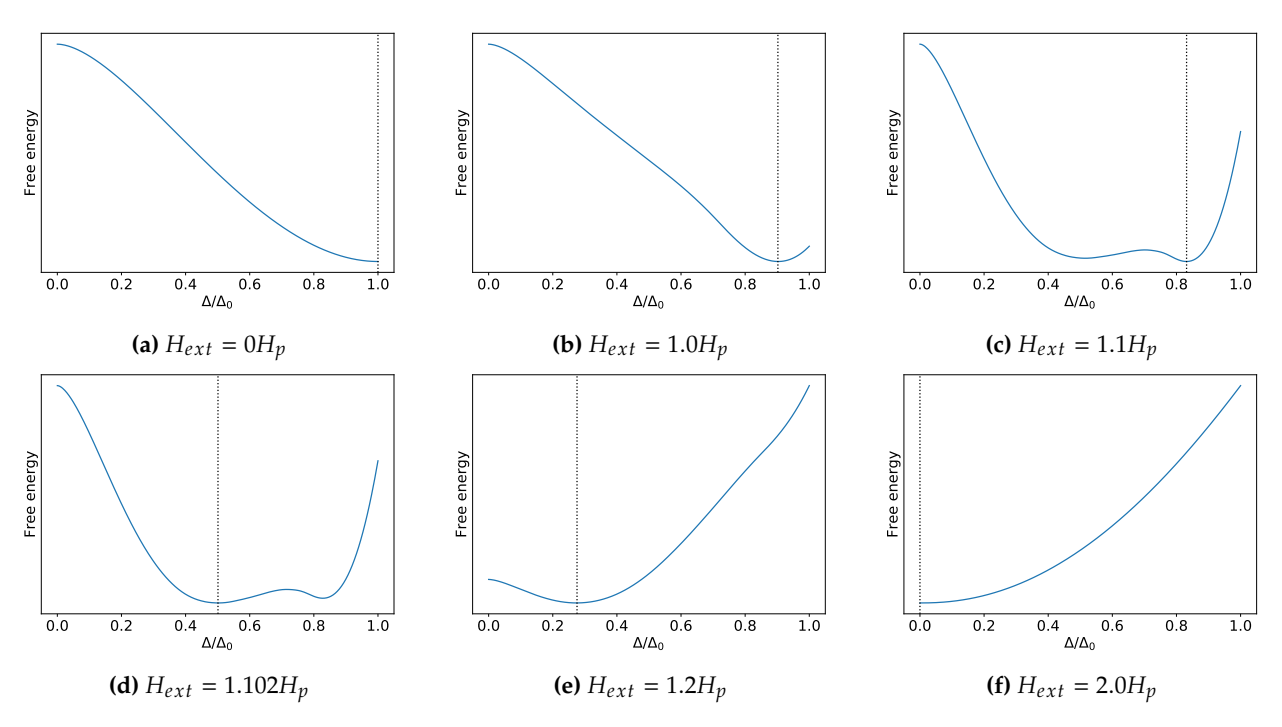


Figure 4.2: Plots of the free energy of MoSe₂ at zero temperature as function of Δ/Δ_0 for $\mu=0.13\,\mathrm{eV}$, $\hbar\omega_D=30\,\mathrm{meV}$, and $\Delta_0=1\,\mathrm{meV}$. A 500×500 equally spaced **k**-point grid is used for these plots and the entire procedure of grid generation is described in section 4.1.2. The vertical dotted line indicates the found global minimum using Brent's algorithm explained in section 4.1.3 and the results are all in agreement with the shown plots. $H_p=\Delta_0/\sqrt{2}$ is the Pauli limit.

4.1.4 Finding the critical field

The last step is to find the critical field as a function of μ and Δ_0 . In order to find this critical field, one need to find for which external field H_{ext} , the superconducting pairing Δ will vanish. Since Δ should decrease when the external fields increases, the critical field can be found with a root-finding algorithm. The algorithm that is considered to be the most efficient is also from Brent and is described in chapter 4 of his book [37]. In python, the algorithm is already implemented in the Scipy library under the name scipy optimize brentq. By doing this process for several chemical potential and Δ_0 , a plot of the critical field as function of chemical potential and Δ_0 can be made. A demonstration of the root-finding algorithm to find the critical field for MoS2 is displayed in fig. 4.3. An equally spaced 500×500 k-point grid has been used for the calculation. Furthermore $\hbar \omega_D = 30$ meV and $\Delta_0 = 1$ meV. The obtained critical fields (vertical dotted lines in the figures) are consistent with the plots of Δ as a function of the external field.

4.2 Analysis of model

4.2.1 Practical input values

In the numerical model presented in section 4.1, the input parameters are the temperature T, the external field H_{ext} , the chemical potential μ , the superconducting pairing at zero temperature and magnetic field Δ_0 , the cutoff energy $\hbar\omega_D$, and the size of the equally spaced **k**-point grid. The highest relevant temperature (i.e. the critical temperature) is related to Δ_0 . In the weak-coupling limit, it is known that Δ_0 and the critical temperature are related by eq. (3.33). According to Lu et al., the maximum critical temperature of MoS₂ is around 10 K [18]. If the weak-coupling limit can be applied to TMD monolayer superconductors, then $\Delta_0 \approx 1.5$ meV. According to Peng et al., the Debye energy of MoS₂ is 22.6 meV [38], which looks consistent with the requirement that $\hbar\omega_D \gg \Delta_0$ for weak-coupling superconductors. In a more recent experiment by Shi et al., it has been found that MoSe₂ has a maximum critical temperature of 7.1 K [39], which comes down to a superconducting pairing of $\Delta_0 \approx 1.1$ meV in the weak-coupling limit. The Debye energy of MoSe₂ is 15.3 meV according to Peng et al., so it is also arguable that MoSe₂ can be described as a weak-coupling superconductor. However, in order to conclude whether the Debye energy is high enough for the weak-coupling limit, one need to consider if the

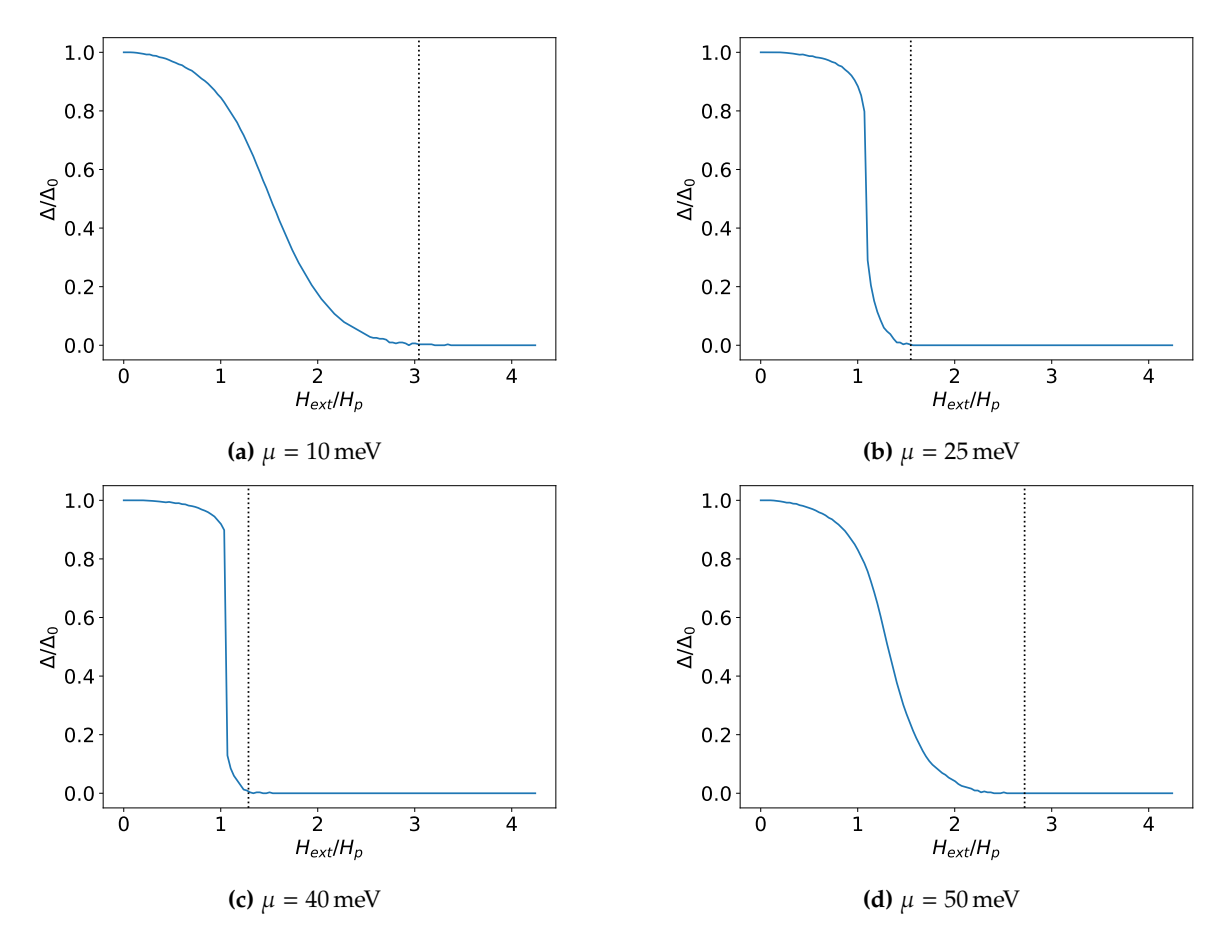


Figure 4.3: Demonstration of root finding algorithm to find the critical field for MoS₂ at several chemical potential. $H_p = \Delta_0/\sqrt{2}$ indicates the Pauli limit. Calculations are done for an equally spaced 500×500 **k**-point grid, and $\hbar\omega_D = 30$ meV, and $\Delta_0 = 1$ meV. The vertically dotted lines in the figures indicate the critical fields according to the root-finding algorithm and are consistent with the plots of Δ as function of the external field.

value of Δ is sufficiently converged, which is explained in more detail in the next section.

4.2.2 Convergence in the weak coupling limit

In this thesis, the cutoff energy is equal to the Debye energy $\hbar\omega_D$. In some reports, however, the cutoff energy is set to a finite number of times the Debye energy (e.g. 3 times [40, 41]). In the weak-coupling limit when the cutoff energy energy diverges, the Δ that minimizes the free energy should converge to a specific value. This means that in this limit, it should not matter how large the cutoff energy is as long as it is much larger than the maximum superconducting pairing Δ_0 . In fig. 4.4, the convergence of Δ is demonstrated for MoSe₂ at $\mu = 0.15\,\text{eV}$. It can been seen that Δ will indeed converge for large cutoff energies that are several times Δ_0 , although noise will be visible if the number **k**-points is too low. This is in particular the case when one approaches the critical field (compare figs. 4.4b and 4.4c).

4.2.3 Uncertainty analysis

As shown in fig. 4.4, the value of Δ that minimizes the free energy has an uncertainty depending on the resolution of the **k**-point grid. The question is how high the resolution of the **k**-point grid should be in order to make the uncertainty acceptably low. As it can be very time consuming to calculate the uncertainty of the critical field for every Δ_0 and μ , it is better to have an upper bound of the uncertainty given the upper and lower bound of μ and Δ_0 . This suggest the following procedure to determine the maximum uncertainty as function of the resolution of the **k**-point grid: for a given material with a given μ and Δ_0 , calculate the critical field for several random cutoff energies $E_D \gg \Delta_0$. The uncertainty can then be determined by computing the standard deviation of the found critical fields. This process will be done for all combinations of boundary values of μ and Δ_0 and in the end, one will simply pick the combination with the highest uncertainty.

The goal now is to find the minimum resolution of the k-point grid such that the relative uncertainty of the critical field is below a certain value. In this thesis, it will be assumed that a relative uncertainty of 0.05 (5%) is acceptable. The calculated uncertainties as function of the resolution for MoSe₂ are displayed in fig. 4.5. This is

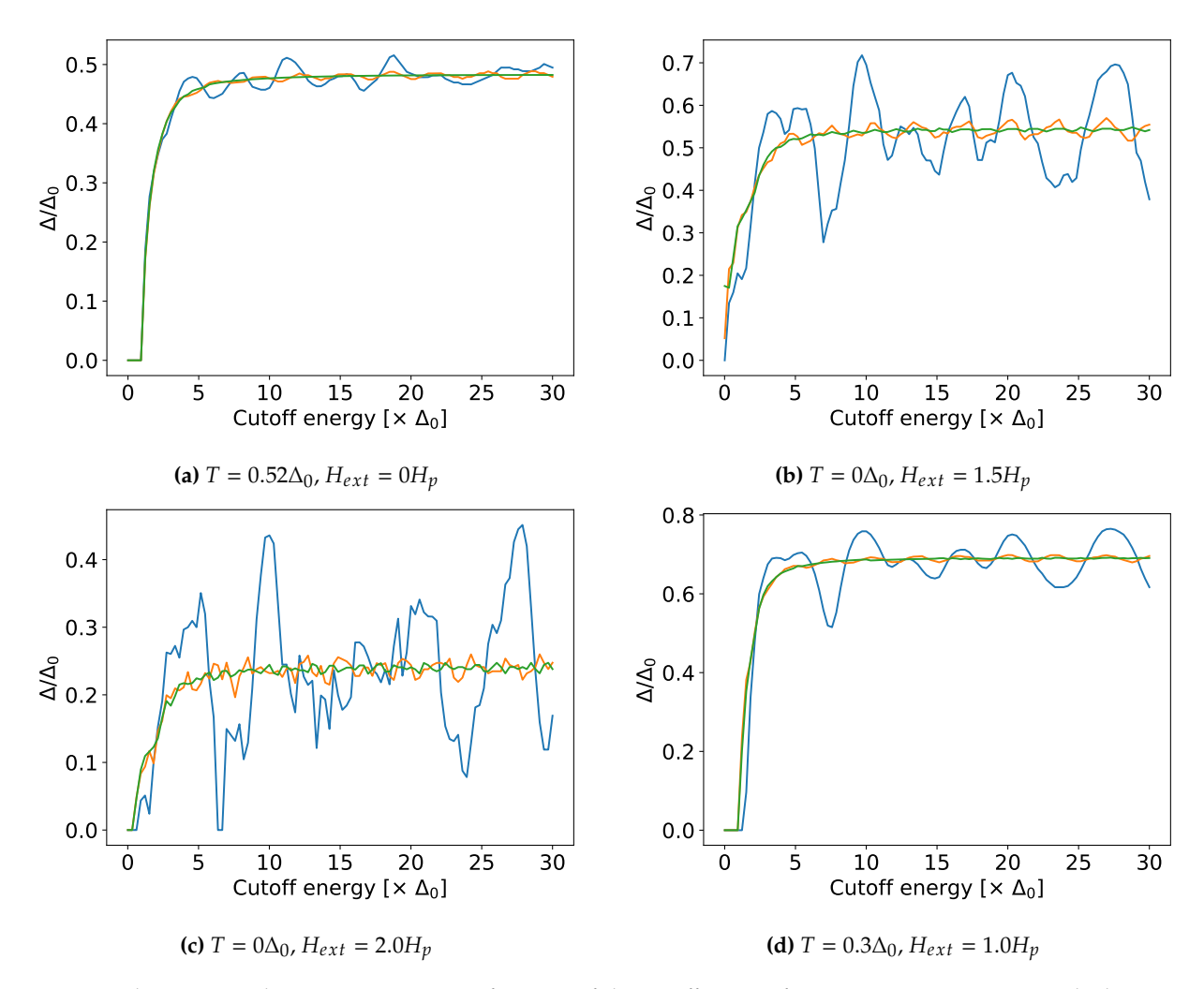


Figure 4.4: The superconducting pairing Δ as a function of the cutoff energy for MoSe₂ at $\mu = 0.15\,\text{eV}$. Calculations are done with a 100×100 (blue), 250×250 (yellow), and 500×500 (green) **k**-point grid. Again $H_p = \Delta_0/\sqrt{2}$ is the Pauli limit.

done by picking 12 random cutoff energies using an uniform distribution on the interval [$15\Delta_0$, $20\Delta_0$], and then calculate the relative uncertainty by dividing the standard deviation by the mean. Comparing fig. 4.5e with the others, it can been seen that the highest uncertainty is at $\mu = 134$ meV and $\Delta_0 = 0.1$ meV. It should be noted that this chemical potential is centered within the vanishing region of MoSe₂. From fig. 4.5e, it appears that a 1000×1000 k-point grid is sufficient in order to obtain a relative uncertainty below 5% for the calculated critical field of MoSe₂. Also for other materials, the highest uncertainty can be found for low Δ_0 and for a chemical potential centered in the vanishing region. It can be argued that a 600×600 k-point grid is sufficient for MoS₂ and a 1200×1200 k-point grid is sufficient for MoTe₂ (see fig. B.1 in appendix B).

4.2.4 Free electron case

As discussed in section 3.2.1, it is expected that the critical field in case of 2D free electrons should reach the Pauli limit (see eq. (3.43)). Moreover, one should also expect to find that the critical temperature is given by eq. (3.33). The presented numerical $\mathbf{k} \cdot \mathbf{p}$ model can be reduced to a free electron model by setting $A \approx 3.81 \, \text{eV} \, \text{Å}^{-2}$ and B = C = D = 0. Plots of the critical field and temperature of the model as well as the analytical expressions (eqs. (3.33) and (3.43) respectively) are shown in fig. 4.6. During the calculation, $\mu = 0.1 \, \text{eV}$, $E_D = 15\Delta_0$, and the size of the \mathbf{k} -point grid is 500×500 . It can be seen in this figure that the results of the model are in good agreement with the analytical expressions.

4.3 Results and discussion

4.3.1 Critical field

Using the procedure described in section 4.1 and the desired resolutions discussed in section 4.2.3, the critical field diagrams are calculated and displayed in fig. 4.7. For every chemical potential μ and maximum super-

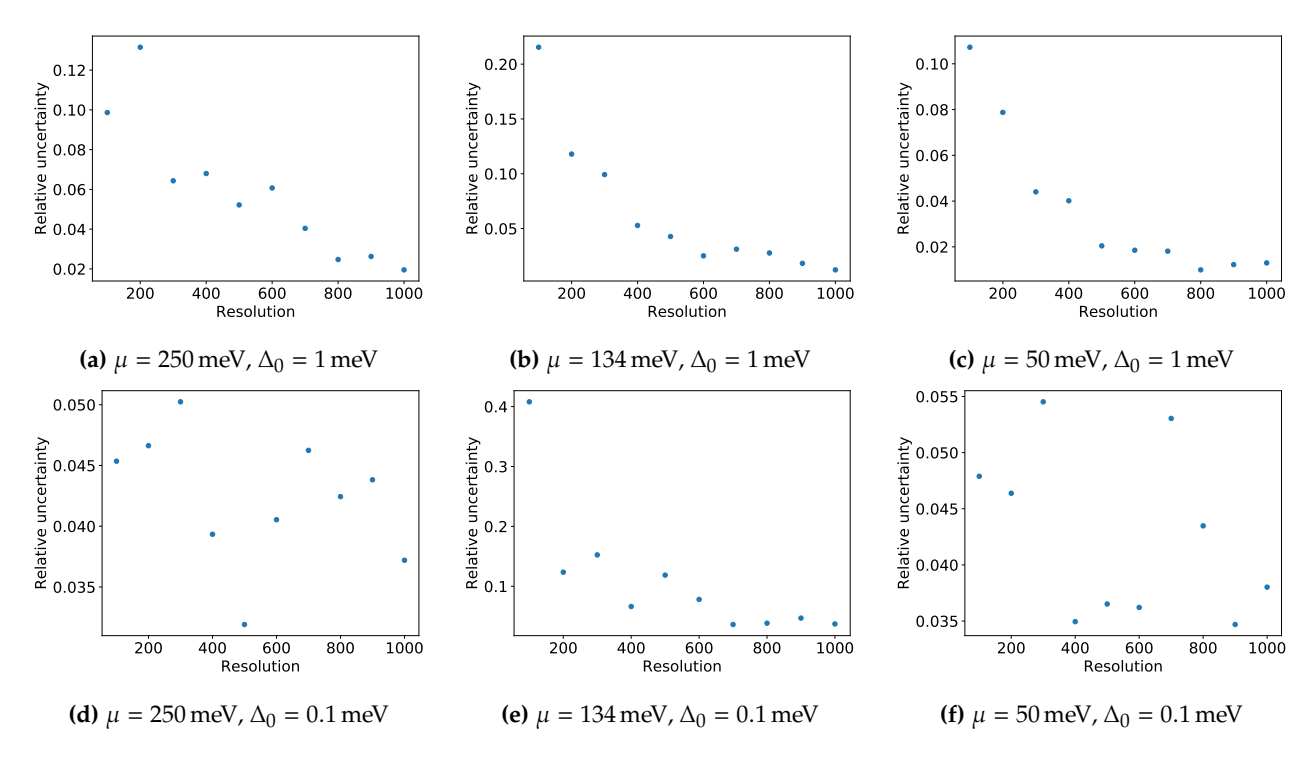


Figure 4.5: The relative uncertainty of the critical field as a function of the resolution for MoSe₂. A resolution of n means that an $n \times n$ **k**-point grid has been used.

conducting pairing Δ_0 , a separate **k**-point grid has been generated and a cutoff energy of $15\Delta_0$ has been used in the calculations. The white dotted lines in the figure indicate the vanishing region given in table 4.2. The figures confirm that the critical field will be suppressed when the chemical potential approaches the vanishing region. Furthermore, it can also be seen that the critical field is lower for lower Δ_0 . However, the critical field with respect to the Pauli limit H_c/H_p is higher for lower Δ_0 . This may be the effect of the SOI, which contributes to the critical field without any Δ_0 dependence. An other remarkable feature is that the critical field will be completely suppressed to (virtually) the Pauli limit in case of MoS₂. This can be explained from the fact that the spin-orbit interaction of MoS₂, compared to the other materials, is very weak at the bottom of the conduction band. For MoSe₂ and MoTe₂, there is a dark strip visible near $\mu = 0$. This is likely the effect of the higher energetic spin-down band at the +K point (and the spin-up band at the -K point) as the strip is located at $\mu = B$ in both cases.

Using the results in fig. 4.7, one can now make a prediction of the critical field in experiments. Previous experiments have shown that the critical temperature (and thus Δ_0) depends on the carrier density in the lowest conduction band (and thus the chemical potential). Thus, for each material, a trajectory through the diagram in fig. 4.7 can be associated with. Ye et al. and Lu et al.[18, 42] have shown that MoS₂ will become superconducting if the carrier density in the conduction band exceeds 6×10^{13} cm⁻². If the effect of spin-orbit interaction is negligible, the corresponding chemical potential can be calculated by

$$\mu \approx A\pi n,$$
 (4.8)

where A is the $\mathbf{k} \cdot \mathbf{p}$ parameter discussed in section 3.2.2 and n the carrier density. Therefore, the minimum chemical potential required to obtain superconducting MoS₂ is given by $\mu_c = 153 \,\mathrm{meV}$, and this will be called the critical chemical potential. Critical chemical potentials are also indicated in fig. 4.7 with red solid lines. From Shi et al.[39], it can be found that the critical carrier density for MoSe₂ is $8 \times 10^{13} \,\mathrm{cm}^{-2}$, which results in a critical chemical potential of 160 meV. However, this value may be overestimated, because the temperature of the experiment did not go below 2 K. A calculation in a more recent experiment by Miao et al.[43] suggests that the critical density is rather roughly $6 \times 10^{13} \,\mathrm{cm}^{-2}$, the same value as for MoS₂. This implies critical chemical potential of 120 meV which is just below the vanishing region (see also fig. 4.7e). Furthermore, Shi et al. suggest that the critical density of MoTe₂ has to be at least $7 \times 10^{13} \,\mathrm{cm}^{-2}$ as no superconductivity has been found for this maximum carrier density. Again, this value may be overestimated due to the fact the experiment did not go below 2 K. If the critical carrier density is the same as for MoS₂ and MoSe₂, then the corresponding critical chemical potential for MoTe₂ is 116 meV, well below the vanishing region (see fig. 4.7f).

Due to the fact that the critical chemical potential of MoS_2 is above the vanishing region, one does not expect to see a drop of the critical field for these two materials. Data from the supplementary data of Ye et al. (figure S3b)

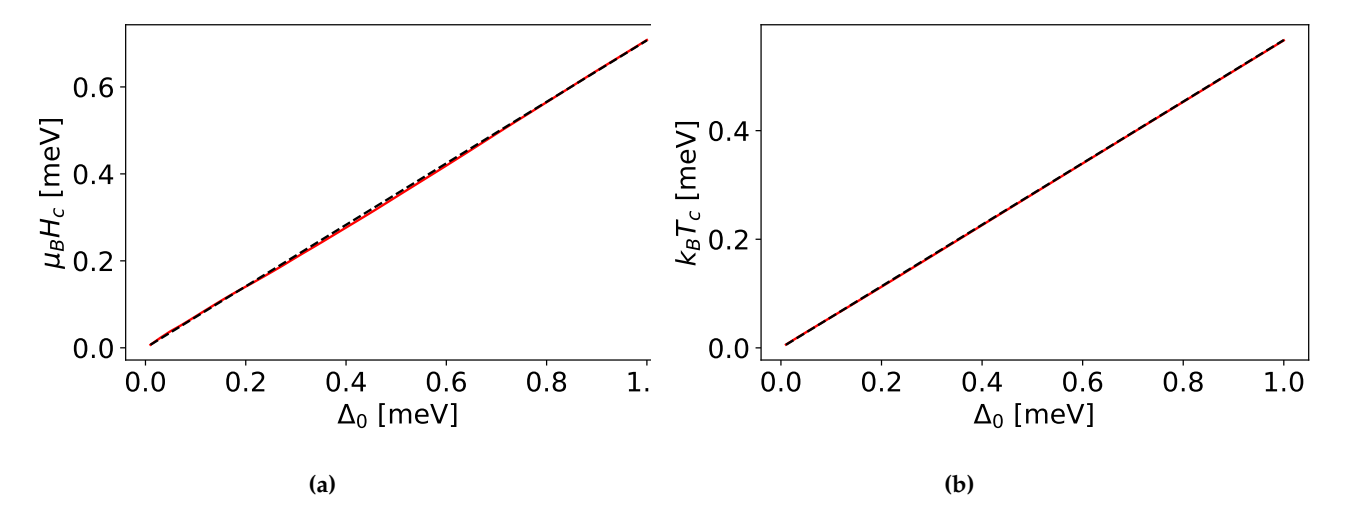


Figure 4.6: The critical field (a) and temperature (b) as a function of Δ_0 in the free electron case. The red lines are computed using the numerical $\mathbf{k} \cdot \mathbf{p}$ model, while the black dashed lines are the analytical expressions discussed in section 3.1. Calculation is done for $\mu = 0.1 \, \text{eV}$, $E_D = 15\Delta_0$, and a $500 \times 500 \, \mathbf{k}$ -point grid.

also confirm this. For $MoSe_2$, the critical carrier density is seemingly 8×10^{13} meV in Shi et al.'s experiment, which results in a critical chemical potential above the vanishing region. The supplementary data of the critical field in Shi et al. (figure S5c) also confirms this as there is no drop of critical field visible in the dome. However, for a lower temperature, it may be possible to get the critical chemical potential below the vanishing region. In that case, it would be expected to see a suppression of the critical field.

4.3.2 Topological phase diagram

4.3.3 Varying chemical potential and critical field, fixed temperature

The topological phase diagram for MoTe₂ at a fixed temperature of 2 K is shown in fig. 4.8. All the calculations are done for $\Delta_0 = 1$ meV, and $E_D = 15\Delta_0$. Furthermore, the resolution of the **k**-point grid was 500×500 for all calculations. The reason why 2 K has been chosen instead of 0 K is that it is very difficult to accurately determine the transition of superconducting phase to normal phase when at 0 K. Consistent with figure 1b in Wang et al.[19], the twelve nodal point topological superconductivity can only be obtained when the chemical potential is inside the vanishing region. Furthermore, one does need an external field energy $\mu_B H_{ext}$ of approximately 0.8 meV to obtain the topological phase. The six nodal point topological superconducting phase is visible near the boundaries of the vanishing region. Figure 4.8 also makes clear that only close to the vanishing region, nodal topological superconductivity is present.

4.3.4 Varying temperature and critical field, fixed chemical potential

Topological phase diagrams for different materials and chemical potential are shown in fig. 4.9. All the calculations are done for $\Delta_0 = 1 \,\text{meV}$, and $E_D = 15\Delta_0$. Furthermore, the resolution of the k-point grid was 500×500 for all calculations. Figures 4.9a to 4.9c show the phase diagram of the three materials mentioned in section 4.1.1 in case the chemical potential lies (approximately) in the middle of the vanishing region. In that case, the trivial topological phase becomes a twelve nodal point topological superconducting phase when the field is sufficiently increased. This can be explained from figure 1b in Wang et al.[19] or eq. (3.57): when the the chemical potential is in the middle of the vanishing region, the material will be in the twelve nodal point topological superconducting phase when

$$0 < H_{ext}^2 - \Delta (H_{ext})^2 < \left(\frac{\mu_{max} - \mu_{min}}{2}\right)^2. \tag{4.9}$$

Otherwise, the material is in the trivial superconducting phase when $\Delta > 0$ and in the normal phase when $\Delta = 0$. Note that $\Delta(H_{ext})$ decreases as the external field increases. Figures 4.9a to 4.9c also show that strength of the spin-orbit interaction has a significant effect on the topological phase diagram. It can clearly be seen that a nodal topological superconducting phase is much easier to obtain in materials with a higher SOI like MoTe₂.

In case the chemical potential is not centered in the vanishing region, the material may also be in the six nodal point topological superconducting phase if the external field is enhanced even more (fig. 4.9d). However, this does not mean that this phase will always be visible as Δ may become zero before $\sqrt{H_{ext}^2 - \Delta(H_{ext})^2}$ is large

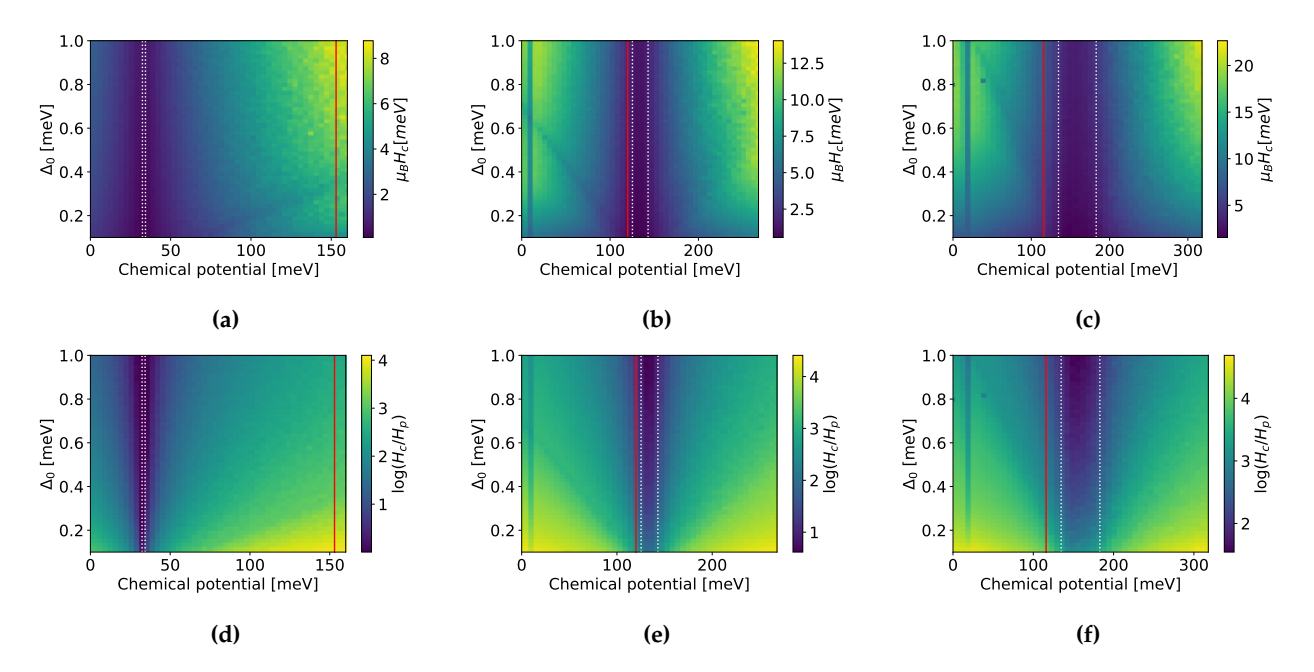


Figure 4.7: Critical field diagrams for (a,d) MoS₂, (b,e) MoSe₂, and (c,f) MoTe₂ as function of chemical potential and Δ_0 . In accordance with the discussion in section 4.2.3, the used resolutions for the calculations are 600×600 , 1000×1000 and 1200×1200 respectively. For every μ and Δ_0 , a separate **k**-point grid has been generated and the cutoff energy is set to $E_D = 15\Delta_0$. The white dotted lines indicate vanishing region based on the values in table 4.2 and the red solid line indicate the critical chemical potential. The diagrams in (a), (b), and (c) show the actual value of the critical field, while the diagrams in (d), (e), (f) show the log of critical field with respect to the Pauli limit H_p .

enough. Once the chemical potential lies outside the vanishing region, it is not possible that the material is in the twelve nodal point topological superconducting phase (fig. 4.9e). The material may be in the six nodal point topological phase when

$$\Delta \mu < \sqrt{H_{ext}^2 - \Delta (H_{ext})^2} < \Delta \mu + \mu_{max} - \mu_{min}, \tag{4.10}$$

where $\Delta\mu$ is the nearest distance of the chemical potential from the vanishing region. As the minimum value of $\Delta\mu$ for nodal topological superconductivity increases faster than the energy of the critical field, no nodal topological superconductivity will be visible when $\Delta\mu$ is high enough (fig. 4.9f). Thus, nodal topological superconductivity is only acquirable when the chemical potential is in or close to the vanishing region.

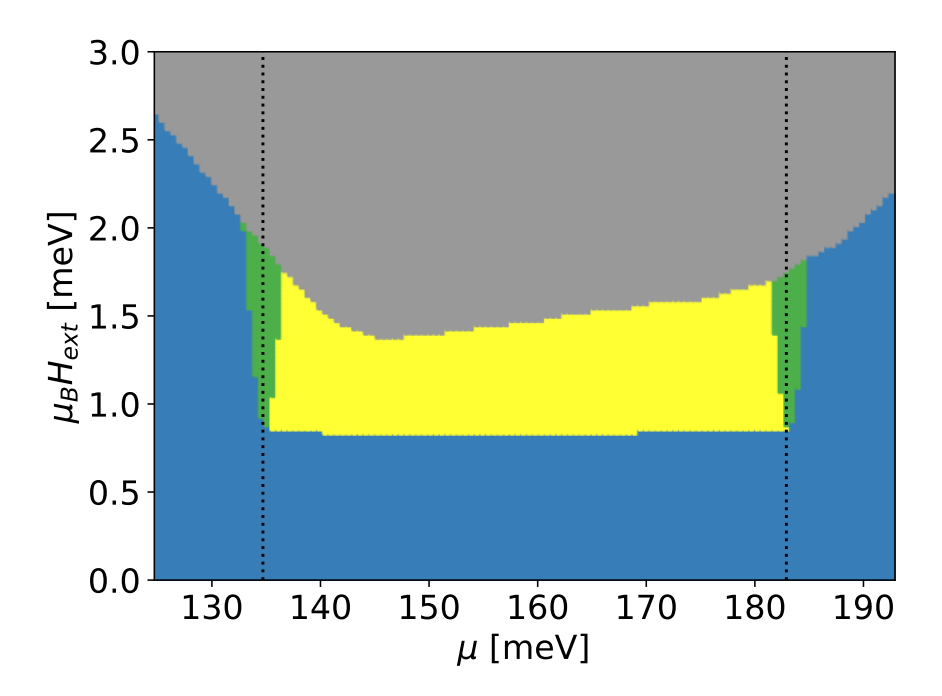


Figure 4.8: Topological phase diagram of MoTe₂ at 2 K. The possible phases are: trivial superconducting phase (blue); twelve nodal point topological superconducting phase (yellow); six nodal point topological superconducting phase (green); normal phase (gray). All calculations are done with a 500×500 **k**-point grid and for $\Delta_0 = 1$ meV, and $E_D = 15\Delta_0$. The black dashed lines indicate the vanishing region of MoTe₂

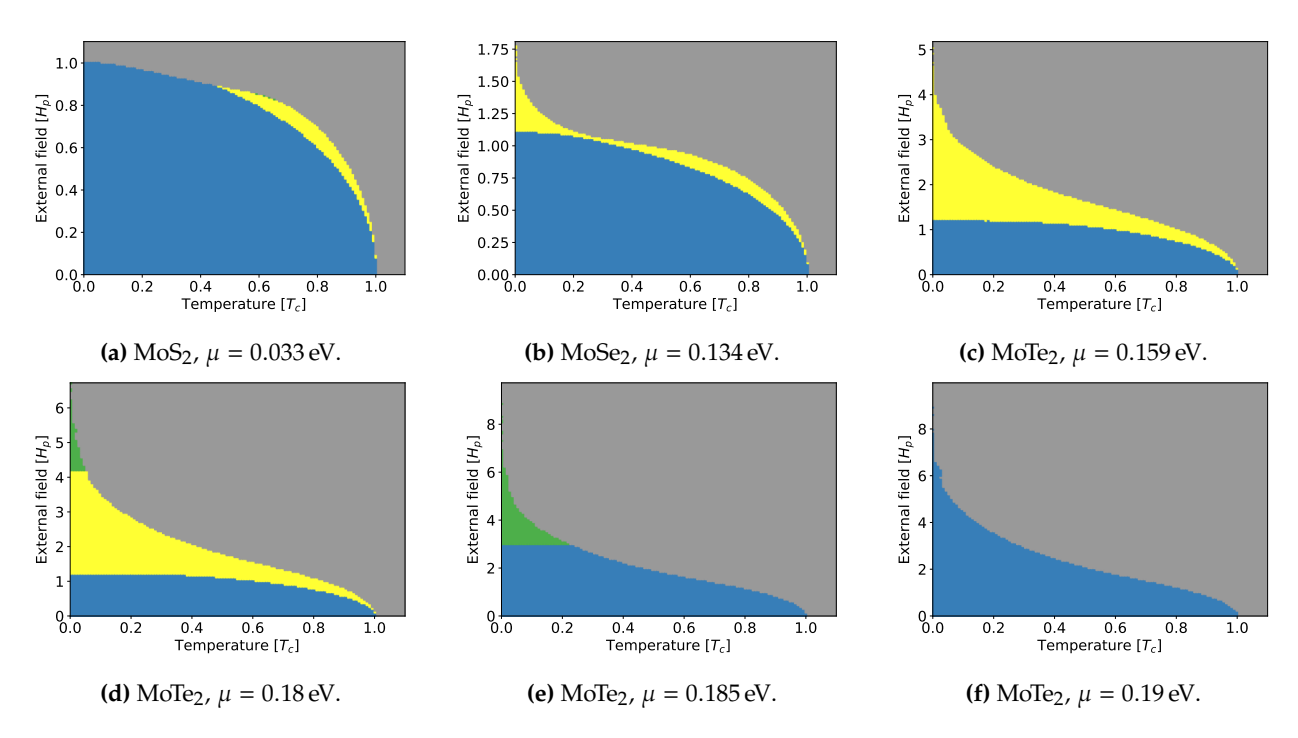


Figure 4.9: Topological phase diagrams for different materials at different chemical potential. The possible phases are: trivial superconducting phase (blue); twelve nodal point topological superconducting phase (yellow); six nodal point topological superconducting phase (green); normal phase (gray). All calculations are done with a 500×500 k-point grid and for $\Delta_0 = 1$ meV, and $E_D = 15\Delta_0$. H_p denotes the Pauli limit while T_c denotes the critical temperature defined in eq. (3.33).

Chapter 5

Conclusion

In this thesis, it has been shown that the critical field with respect to the Pauli limit is expected to drop when the vanishing region is approached. This drop, however, can only be seen if the critical chemical potential is below the vanishing region. For MoS_2 , this is not the case and it is therefore not expected to see a suppression of the critical field. For $MoSe_2$, it is possible to have a critical chemical potential below the vanishing region, but this requires temperatures to be below 2 K. For $MoTe_2$, it is not clear what the actual critical chemical potential is, but if the critical carrier density is the same as for MoS_2 , then a suppression of the critical field is expected. The critical field diagrams are based on the $\mathbf{k} \cdot \mathbf{p}$ model, which is accurate as long as the chemical potential is not too high so that the effect of other conduction band minima is negligible.

In this thesis, it has also been shown that nodal topological superconducting phase can be acquired when the chemical potential is within or not too far away from the vanishing region. This means that it is only possible when there is superconductivity for a chemical potential near the vanishing region, and this is not the case for MoS_2 . $MoSe_2$ and $MoTe_2$, on the other hand, are more suitable candidates to show nodal topological superconductivity as the critical chemical potential may lie below the vanishing region. Nodal topological superconductivity, however, is easier to show for $MoTe_2$ as the SOI is stronger, causing a higher critical field.

Bibliography

- 1. Kokalj, A. Journal of Molecular Graphics and Modelling 17, 176–179 (1999).
- 2. Novoselov, K. S. et al. Science 306, 666–669 (2004).
- 3. Novoselov, K. S. et al. Proceedings of the National Academy of Sciences 102, 10451–10453 (2005).
- 4. Mak, K. F. et al. Physical Review Letters 105, 136805 (2010).
- 5. Splendiani, A. et al. Nano Letters 10, 1271–1275 (2010).
- 6. Magda, G. Z. et al. Scientific Reports 5, 14714 (2015).
- 7. Choi, W. et al. Materials Today 20, 116–130 (2017).
- 8. Wilson, J. & Yoffe, A. Advances in Physics 18, 193–335 (1969).
- 9. Bromley, R. A., Murray, R. B. & Yoffe, A. D. Journal of Physics C: Solid State Physics 5, 759 (1972).
- 10. Mattheiss, L. F. Physical Review B 8, 3719–3740 (1973).
- 11. Radisavljevic, B. et al. Nature Nanotechnology 6, 147–150 (2011).
- 12. Lopez-Sanchez, O. et al. Nature Nanotechnology 8, 497–501 (2013).
- 13. Zeng, H. et al. Nature Nanotechnology 7, 490–493 (2012).
- 14. Yao, W., Xiao, D. & Niu, Q. Physical Review B 77, 235406 (2008).
- 15. Rycerz, A., Tworzydo, J. & Beenakker, C. W. J. Nature Physics 3, 172–175 (2007).
- 16. Xiao, D. et al. Physical Review Letters 108, 196802 (2012).
- 17. Kormányos, A. et al. Physical Review B 88, 045416 (2013).
- 18. Lu, J. M. et al. Science **350**, 1353–1357 (2015).
- 19. Wang, L., Rosdahl, T. O. & Sticlet, D. Physical Review B 98, 205411 (2018).
- 20. Liu, G.-B. et al. Physical Review B **88** (2013).
- 21. Groth, C. W. et al. New Journal of Physics 16, 063065 (2014).
- 22. Liu, G.-B. et al. Physical Review B 89, 039901 (2014).
- 23. Cheiwchanchamnangij, T. & Lambrecht, W. R. L. Physical Review B 85, 205302 (2012).
- 24. Zeng, H. et al. Physical Review B 86, 241301 (2012).
- 25. Fang, S. et al. Physical Review B 92 (2015).
- 26. Komider, K., González, J. W. & Fernández-Rossier, J. Physical Review B 88, 245436 (2013).
- 27. Rostami, H., Moghaddam, A. G. & Asgari, R. Physical Review B 88, 085440 (2013).
- 28. Fröhlich, H. Physical Review 79, 845–856 (1950).
- 29. Bardeen, J., Cooper, L. N. & Schrieffer, J. R. Physical Review 108, 1175–1204 (1957).
- 30. Clogston, A. M. Physical Review Letters 9, 266–267 (1962).
- 31. He, W.-Y. et al. Communications Physics 1 (2018).
- 32. Bogoljubov, N. N. Il Nuovo Cimento (1955-1965) 7, 794–805 (1958).
- 33. Valatin, J. G. Il Nuovo Cimento (1955-1965) 7, 843-857 (1958).
- 34. Tinkham, M. 2nd ed. (Dover Publications inc., Mineola, New York, 1996).
- 35. Kormányos, A. et al. 2D Materials 2, 022001 (2015).
- 36. Löwdin, P. The Journal of Chemical Physics 19, 1396–1401 (1951).
- 37. Brent, R. P. (Prentice-Hall, Englewood Cliffs, New Jersey, 1973).
- 38. Peng, B. et al. RSC Advances 6, 5767–5773 (2016).
- 39. Shi, W. et al. Scientific Reports 5 (2015).
- 40. Szczniak, R., Durajski, A. P. & Herok, . Physica Scripta 89, 125701 (2014).
- 41. Carbotte, J. P. Reviews of Modern Physics 62, 1027–1157 (1990).
- 42. Ye, J. T. et al. Science 338, 1193-1196 (2012).
- 43. Miao, X. et al. Scientific Reports **6**, 29292 (2016).

Appendix A

Convergence of Δ that minimizes free energy

To analyze the convergence of Δ in eq. (3.31) when $\hbar\omega_D \to \infty$, one need to find approximate expressions of the left hand side and right hand side for large $\hbar\omega_D$. To start with the left hand side, one can start the expression given in eq. (3.29):

$$\frac{1}{V} = \frac{\mathcal{N}_{tot}(0)}{2} \sinh^{-1} \left(\frac{\hbar \omega_D}{|\Delta_0|} \right)$$

$$= \frac{\mathcal{N}_{tot}(0)}{2} \log \left(\frac{\hbar \omega_D}{|\Delta_0|} \left(1 + \sqrt{1 + \left[\frac{|\Delta_0|}{\hbar \omega_D} \right]^2} \right) \right)$$

$$\approx \frac{\mathcal{N}_{tot}(0)}{2} \log \left(\frac{2\hbar \omega_D}{|\Delta_0|} \right).$$
(A.1)

The right hand side can be approximated by

$$rhs = \frac{N_{tot}(0)}{2} \int_{0}^{\hbar\omega_{D}} \tanh\left(\frac{\sqrt{\xi^{2} + |\Delta|^{2}}}{2k_{B}T}\right) \frac{d\xi}{\sqrt{\xi^{2} + |\Delta|^{2}}}$$

$$\approx \frac{N_{tot}(0)}{2} \log\left(\frac{\hbar\omega_{D}}{|\Delta|} \left(1 + \sqrt{1 + \left[\frac{|\Delta|}{\hbar\omega_{D}}\right]^{2}}\right)\right) - C$$

$$\approx \frac{N_{tot}(0)}{2} \log\left(\alpha \frac{2\hbar\omega_{D}}{|\Delta|}\right). \tag{A.2}$$

This approximation can be justified by the fact that $\tanh\left(\sqrt{\xi^2+|\Delta|^2}/2k_BT\right)\to 1$ when $\xi\to\hbar\omega_D\to\infty$.

However, as the integral also involves low energies for which the tanh term is less than 1, one need to subtract a constant C>0 that is independent from $\hbar\omega_D$. The independence of C from $\hbar\omega_D$ is justified by the fact that it is much larger than the Boltzmann energy k_BT . This constant can be rewritten as an other constant $\alpha=\exp(-C)<1$ inside the log. From eqs. (A.1) and (A.2), it can be seen that both sides of eq. (3.31) will grow logarithmic with respect to $\hbar\omega_D$. It can also be seen that $|\Delta|$ will converge to $\alpha|\Delta_0|$ in order to balance the equation, what was to be shown.

Appendix B

The relative uncertainty for MoS₂ and MoTe₂ as function of resolution

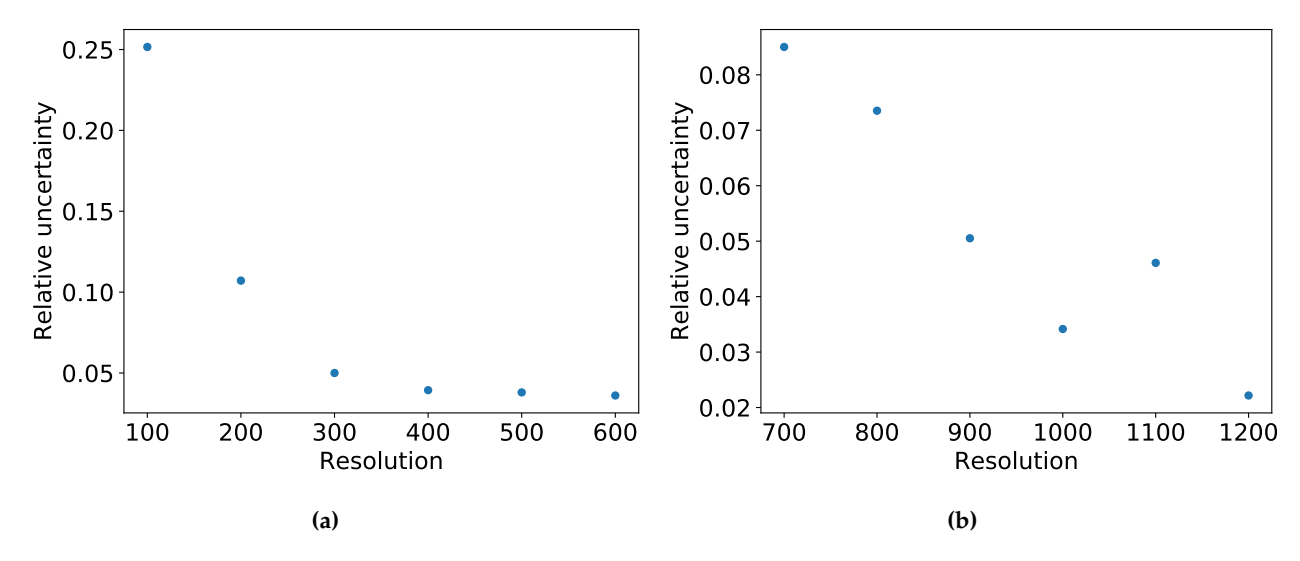


Figure B.1: The relative uncertainty of the critical field as a function of the resolution for (a) MoS₂ and (b) MoTe₂. The chemical potentials are 33 meV and 159 meV respectively and $\Delta_0 = 0.1$ meV for both plots. Just as in the case of MoSe₂, the highest uncertainty can be found for low Δ_0 and at the center of the vanishing point, which is also visualized in the figures. The same procedure explained in section 4.2.3 has been used in order to calculate the relative uncertainties. Furthermore, the figures show that a 600×600 **k**-point grid and a 1200×1200 **k**-point grid are sufficient for MoS₂ and MoTe₂ respectively, in order to be below the upper bound of 5% relative uncertainty. Similar to fig. 4.5, a resolution of n implies an $n \times n$ equally spaced **k**-point grid has been used.